remote sensing

MDPI

Article

High-Resolution Multiscale Seismic Fracture Prediction via Basis Pursuit Frequency Extension-Enhanced Multi-Attribute Fusion

Jun Wang [1], Junxing Cao [1,*] and Yajuan Xue [2]

[1] State Key Laboratory of Oil and Gas Reservoir Geology and Exploitation, Chengdu University of Technology, Chengdu 610059, China; wangjlyy@cdut.edu.cn
[2] School of Communication Engineering, Chengdu University of Information Technology, Chengdu 610225, China
* Correspondence: caojx@cdut.edu.cn

Highlights

What are the main findings?

- Basis pursuit frequency extension broadens the effective seismic bandwidth without estimating the actual seismic wavelet. Synthetic tests with known reflectivity quantify its spectral, phase, amplitude and thin-bed fidelity, noise robustness and parameter sensitivity.
- Structure-tensor-guided coherence and ant tracking are sensitive to complementary large- and small-scale discontinuities (attribute-sensitive scales), which are integrated into multiscale predictions through normalized weighted fusion.

What are the implications of the main findings?

- The results show that the proposed workflow is feasible and effective, producing fracture images that are clearer, more detailed and more consistent with the actual geological understanding than single-attribute or conventional fusion results.
- The workflow supports weak-response small-fracture characterization, reservoir sweet-spot prediction and well-location optimization in tight reservoirs, although further validation with independent datasets is required.

Abstract

Fractures are important storage spaces and flow pathways in tight reservoirs, but small-scale fractures with weak seismic responses are difficult to characterize with band-limited post-stack seismic data. This study proposes a high-resolution multiscale seismic method for predicting fracture distribution based on basis pursuit frequency extension (BPFE)-enhanced multi-attribute fusion. BPFE represents each trace sparsely on a wedge dictionary built from a zero-phase Morlet wavelet, which is derived from the average dominant frequency of the data. It then re-synthesizes the basis pursuit denoising solution with a time-compressed wavelet, thereby extending the effective bandwidth without estimating the seismic wavelet. Dip-steered third-generation coherence and ant-tracking attributes are subsequently normalized and fused with explicit weights according to their attribute-sensitive scales, and objective rules are provided for selecting the BPFE parameters. Synthetic tests with known reflectivity show that BPFE reproduces the ideal high-resolution section with correlation coefficients of 0.978 (noise-free) and 0.882 (signal-to-noise ratio of 10 dB). BPFE increases the dominant frequency from 30.8 to 49.3 Hz and reduces the tuning thickness from 16 to 11 ms without systematic phase rotation. At 10 dB, it also raises the area under the receiver operating characteristic curve for detecting weak bed-confined discontinuities from 0.580 to 0.687, outperforming spectral whitening, spiking deconvolution, inverse-Q filtering and sparse-spike inversion in this respect. Applied to the tight sandstone reservoir

Check for updates

Academic Editor: Dedalo Marchetti

Received: 19 August 2026
Revised: 13 October 2026
Accepted: 14 October 2026
Published: 16 October 2026

Copyright: © 2026 by the authors. Licensee MDPI, Basel, Switzerland. This article is an open access article distributed under the terms and conditions of the Creative Commons Attribution (CC BY) license.

in the northeastern Sichuan Basin, the workflow delineates main faults, fault-associated fracture zones and small-scale discontinuities more completely than coherence, ant tracking or their fusion without BPFE, which is consistent with the actual geological understanding. The workflow offers a wavelet-estimation-free approach for characterizing weak-response small-scale fractures, although its generalization requires further field validation.

Keywords: multiscale fracture characterization; basis pursuit frequency extension; sparse representation; gradient structure tensor; multi-attribute fusion; coherence analysis; ant tracking

1. Introduction

With the development of the global hydrocarbon industry and the profound reshaping of the energy landscape, oil and gas exploration and production are rapidly expanding into deep-earth, deep-water, and unconventional domains [1,2]. These domains are the main frontiers for current growth in hydrocarbon reserves and production, and their reservoirs contain diverse types of fractures with different degrees of development [3–5]. Fractures are important reservoir spaces and seepage channels in tight oil and gas reservoirs, such as deep sandstone and carbonate reservoirs [6,7]. Natural fracture systems of different types and origins control the degree of hydrocarbon enrichment and are key factors determining whether a reservoir can achieve high and stable productivity [8–10]. Therefore, clarifying fracture development and spatial distribution is of great significance for identifying sweet spots in tight oil and gas reservoirs, optimizing well patterns and formulating water control strategies during production. However, effective fracture prediction remains difficult, especially for small-scale fractures. This difficulty stems from the complex genesis of fractures, the diversity of controlling factors, the randomness of fracture formation and development, and the heterogeneous and multiscale nature of their spatial distribution.

Fault and fracture prediction using geological and geophysical information such as seismic and logging data has long been a major objective in hydrocarbon exploration and production, and it has received extensive attention [10–18]. Many seismic-based fracture prediction methods are currently available, and they can generally be divided into pre-stack and post-stack categories according to the type of data used [10,13,19–23]. Pre-stack methods mainly invert fracture parameters from the azimuthal dependence of seismic waves in anisotropic media [24–27] or characterize fracture features using shear-wave splitting [28,29]. However, their broader application has been greatly limited by the high cost of data acquisition and processing, strict application conditions, and difficulties in exciting pure shear waves. In contrast, post-stack methods mainly use three-dimensional (3D) seismic attributes to predict fracture parameters in formations. In other words, they characterize reservoir fractures using the geometric attributes of seismic data volumes [13,30,31]. Seismic attributes can reflect abnormal changes in amplitude, dip, and reflector continuity in seismic data and are commonly used to identify fault structures and predict the spatial distribution of fractures. Considering applicability, data availability and prediction accuracy, seismic attribute analysis remains the most widely used approach for predicting the development and spatial distribution of fractures [32–35].

Seismic attribute analysis methods, such as coherence analysis, curvature analysis and ant tracking, are widely used in fracture prediction because they are economical, convenient and broadly applicable. Curvature attributes identify curvature variations in geological bodies, thereby allowing effective characterization of structures such as stratal bending, faulting and folding, as well as predicting fracture development [36,37]. However,

the basic assumption of curvature-based fracture prediction is that a monotonic mapping relationship exists between structural deformation and fracture development. Therefore, curvature attributes are not applicable to fractured areas without obvious structural features [13]. Coherence attributes characterize discontinuity features in strata by directly measuring lateral amplitude and waveform changes caused by structural discontinuities, stratigraphic discontinuities, and pinch-outs in seismic data [33,38–40]. Thus, this approach performs well in characterizing large- to medium-scale fractures that can be effectively resolved by seismic data [41]. Nevertheless, the linear outlines of fractures identified using coherence and curvature attributes are often not sufficiently clear [41–43]. Moreover, secondary faults associated with fracture zones may cause localized plastic deformation of strata. This deformation leads to lateral variations in seismic velocity and blurs fault responses in seismic records. Ant tracking is a seismic attribute analysis method based on a bionic algorithm. It simulates the process by which ants find the shortest path in nature and performs excellently in enhancing spatial discontinuities and extracting fracture traces [5,44–48]. Ant-tracking attributes reduce the step-like artifacts caused by non-fault factors (e.g., stratigraphic superposition) in geometric attribute volumes such as coherence and curvature [35,41,49]. Consequently, they significantly improve the clarity of small- to medium-scale fracture prediction.

The inherent multiscale nature and strong heterogeneity of fracture formation and distribution make it difficult for any single method to comprehensively delineate the spatial distribution of fracture systems [2,5,10,12,13,23,50]. Moreover, different seismic attributes identify fractures at different scales. It is generally believed that coherence attributes can accurately characterize faults and large- to medium-scale fractures, whereas ant-tracking attributes can effectively depict small- to medium-scale fractures [35,41,48]. Here and throughout this paper, large-scale and small-scale refer to the attribute-sensitive scales of seismic discontinuities, that is, their lateral continuity, vertical extent and discontinuity strength in the seismic image. They do not refer to the physical aperture or length of individual fractures, which are generally far below seismic resolution [13,41]. As noted above, coherence analysis and ant tracking have different sensitivities to fracture scales and are therefore naturally complementary. From this perspective, combining them can overcome their individual limitations while retaining their respective advantages. Accordingly, coherence analysis and the ant-tracking algorithm are combined in this study to capture fault and fracture features from seismic data more comprehensively. Nevertheless, seismic attribute-based fracture prediction is often constrained by the frequency and resolution of seismic data [23,51]. In practice, improving the signal-to-noise ratio of seismic data has become the mainstream approach for enhancing the spatial resolution of seismic attribute-based fracture prediction [32,33,41,52]. However, this process inevitably weakens or even removes subtle seismic variations that carry small-scale fracture information. As a result, the fracture prediction results may be compromised, particularly for small-scale fractures.

The ability of 3D seismic data to identify geological bodies depends on their resolution, and smaller geological targets require higher-resolution seismic data [51,53]. However, because of energy absorption, attenuation and wavelet interference in strata, actual seismic data usually show a narrow bandwidth, blurred features and low resolution [53,54]. These characteristics limit the accuracy of fracture prediction. The effective seismic bandwidth contains different frequency components, and high-resolution processing that enhances high-frequency energy can improve the ability to identify small-scale fractures [51]. Commonly used methods for improving seismic data resolution include deconvolution, inverse Q-filtering, and spectral whitening [55,56]. Deconvolution improves seismic data resolution by compressing wavelets [57,58]. Inverse Q-filtering compensates for the energy attenuation of seismic wavelets caused by formation absorption, thereby extending the frequency

band [59,60]. Spectral whitening flattens the amplitude spectra of seismic records within the effective frequency band to compensate for high-frequency loss, thereby improving resolution [61,62]. However, these methods rely on certain assumptions [56]. For example, inverse Q-filtering assumes a constant-Q formation model, which can hardly reflect the actual conditions of subsurface media. Deconvolution assumes that the reflectivity series follows a Gaussian distribution and that the wavelet is minimum-phase, whereas spectral whitening assumes that the spectrum of the reflectivity series is white. In practice, actual seismic data rarely satisfy these assumptions strictly. These methods also suffer from problems such as difficulty in wavelet extraction, poor noise resistance, and uncertainty in formation Q-factor estimation.

Sparse-representation methods provide another route to resolution enhancement. Based on compressed sensing theory, these methods assume that the reflectivity series is sparse and recover it by ℓ_1-norm-regularized inversion, such as sparse-spike inversion, spectral inversion and basis pursuit inversion [63–65]. The estimated reflectivity can then be re-convolved with a broadband wavelet [63–65]. Basis pursuit inversion with a wedge dictionary is particularly effective for thin layers, because a thin bed is represented by a single dipole atom rather than by two interfering spikes [65]. However, these approaches generally require an explicit estimate of the seismic wavelet (amplitude and phase). Moreover, their output is a reflectivity series whose fidelity depends strongly on the accuracy of this estimate. The basis pursuit frequency extension (BPFE) method adopted in this study belongs to this family but differs in three respects. (1) The dictionary is built from a zero-phase analysis wavelet derived only from the average dominant frequency of the data, so no wavelet extraction or well tie is required. (2) The sparse coefficients are not interpreted as an absolute reflectivity; instead, they are re-synthesized with a time-compressed version of the same analysis wavelet. Thus, the output remains a band-limited seismic record, and its bandwidth extension is explicitly controlled by a single compression coefficient. (3) The basis pursuit denoising (BPDN) formulation, combined with a data-driven regularization rule, accounts for noise in the data. These properties make BPFE suitable as a pre-conditioning step for discontinuity attributes, which require a seismic-like (rather than spiky) input with preserved lateral consistency.

In summary, a multiscale fracture prediction method integrating BPFE and multi-attribute fusion is proposed to address the challenge of multiscale fractures in tight reservoirs. BPFE draws on the BPDN technique for signal reconstruction in compressed sensing. It improves seismic data resolution by projecting seismic records formed by low-frequency wavelets onto records formed by high-frequency wavelets, thereby enhancing the ability of seismic signals to identify small-scale fractures. Coherence attributes effectively characterize the seismic discontinuities caused by large- to medium-scale fractures and can serve as the overall trend constraint for ant-tracking fracture detection. The resulting large- to medium-scale fracture distribution is then fused with the small- to medium-scale ant-tracking results. This fusion characterizes fracture development and spatial distribution at different scales, thereby achieving comprehensive multiscale fracture prediction. The proposed method is applied to field seismic data from the northeastern Sichuan Basin and compared with coherence analysis, ant tracking, and their combined method, while a comprehensive evaluation is conducted together with regional geological understanding and well-log interpretation results. The application results demonstrate that the proposed method is feasible and effective and achieves better identification performance than conventional methods, particularly for small-scale fractures with weak seismic responses.

2. Materials and Methods

This section sequentially presents BPFE-based high-resolution processing, the gradient structure tensor, coherence analysis, ant-tracking technology, the proposed multiscale fracture prediction workflow, and the parameter selection rules and evaluation metrics.

2.1. Basis Pursuit Frequency Extension High-Resolution Processing

Seismic resolution measures the ability of seismic signals to distinguish two adjacent formations, and high-resolution seismic data are beneficial for detecting subsurface geological targets [51,53,55,56]. High-resolution seismic processing is critical for accurately identifying small-scale fractures. However, conventional methods have strict application conditions and require complex estimation of key parameters, which limits their practical application [56]. In BPFE-based high-resolution processing, a low-frequency analysis-specific wavelet sequence is first generated from the estimated average dominant frequency of the seismic data and is then projected onto a high-frequency synthetic analysis wavelet sequence. Next, the sparse representation of the seismic data is reconstructed by BPDN, a compressed sensing reconstruction algorithm. This sparse representation is combined with the synthetic analysis wavelet sequence to reconstruct seismic records with high-frequency wavelets, thereby generating high-resolution seismic data. The BPFE method performs high-resolution processing in a specific sparse domain without calculating the actual seismic wavelet, and it extends the effective bandwidth by a controllable factor. The process is shown in Figure 1, and the steps are as follows:

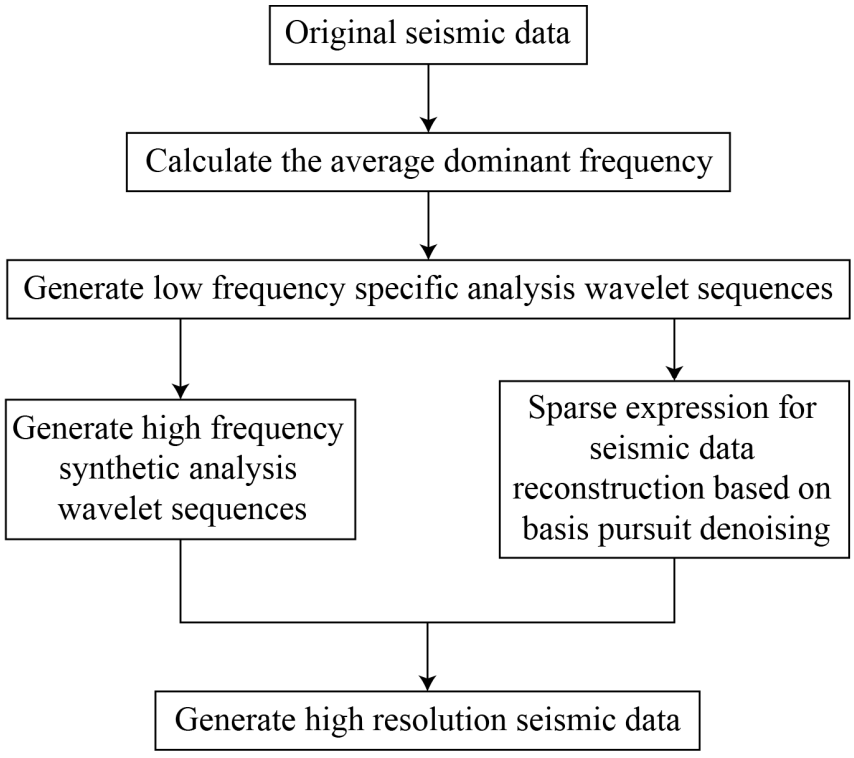


Figure 1. Basis pursuit frequency extension-based seismic high-resolution processing flow.

The average dominant frequency of the seismic data is estimated using the Fourier transform and is then used to generate the low-frequency analysis-specific wavelet sequence. Let x_{MN} denote the original seismic data, where M is the number of seismic traces and N is the seismic trace length. First, the frequency corresponding to the maximum spectral amplitude is calculated trace by trace using the Fourier transform. Then, these

peak frequencies are averaged over all traces to obtain the average dominant frequency f_{ad}, as shown in Equation (1).

$$f_{ad} = \frac{1}{M}\sum_{i=1}^{M}\arg\max_{f}|fft(x_i)| \tag{1}$$

where $fft(\cdot)$ denotes the fast Fourier transform, $\arg\max_f|\cdot|$ returns the frequency at which the amplitude spectrum reaches its maximum, and x_i represents the i-th seismic trace.

On this basis, the average dominant frequency is used to generate the low-frequency analysis-specific wavelet sequence of the seismic data. The analysis wavelet is a zero-phase Morlet (Gaussian-modulated) wavelet [66], denoted as $\omega(t)$, with a center frequency of kf_{ad}, where k is an adjustment factor (its objective selection is described in Section 2.6). $\omega(t)$ is formulated as

$$\omega(t) = \frac{1}{\sqrt{2\pi}\sigma}\exp\left(-\frac{t^2}{2\sigma^2}\right)\exp(j2\pi k f_{ad} t) \tag{2}$$

The corresponding frequency-domain expression is

$$W(f) = \exp[-2\pi^2\sigma^2(f - kf_{ad})^2] \tag{3}$$

where t is time (s), j is the imaginary unit, and σ controls the width of the Gaussian envelope. We set $\sigma = 1/(2\pi\gamma k f_{ad})$, so that the relative bandwidth $\gamma = \sigma_f/(kf_{ad})$ of the wavelet is fixed, where $\sigma_f = 1/(2\pi\sigma)$ is the standard deviation of the Gaussian spectrum in Equation (3). In this study, $\gamma = 0.45$ is used, which gives a wavelet with approximately the same relative bandwidth as a Ricker wavelet. The real part of $\omega(t)$, which is an even (zero-phase) function, is used as the analysis wavelet. It is corrected to zero mean (admissibility condition) and normalized to unit peak amplitude. With this convention, a positive reflection coefficient produces a symmetric central peak. BPFE therefore assumes that the input post-stack data are approximately zero-phase, which is the usual objective of post-stack processing.

Basis pursuit denoising, a compressed sensing reconstruction algorithm, is used to reconstruct the sparse representation of the original seismic data on the low-frequency analysis-specific wavelet sequence [67–69]. Here, the sparse representation of each seismic trace obtained by BPDN is described as:

$$\hat{\mathbf{x}} = \mathrm{argmin}_{\mathrm{x}}\lambda\|\mathbf{x}\|_1 + 1/2\left\|\widetilde{\mathbf{d}} - \mathbf{A}_{MM}\mathbf{x}\right\|_2^2 \tag{4}$$

where λ is the regularization parameter, $\widetilde{\mathbf{d}} \in \mathbb{R}^N$ is the normalized seismic trace with N samples, $\mathbf{x}$ is the vector of sparse coefficients, and $\mathbf{A}_{MM}$ is the observation matrix (dictionary). $\mathbf{A}_{MM}$ contains the wedge model data generated from the analysis wavelet using the dipole model [65]. Each column is the analysis wavelet convolved with a unit single spike or with an even or odd dipole of thickness $m\Delta t$,

$$\mathbf{a}_{i,0} = \mathbf{W}\boldsymbol{\delta}_i,\ \ \mathbf{a}_{i,m}^{\pm} = \mathbf{W}(\boldsymbol{\delta}_i \pm \boldsymbol{\delta}_{i,m}),\ \ m = 1, 2, \ldots, m_{\max} \tag{5}$$

where $\mathbf{W}$ is the convolution matrix of the analysis wavelet, and $\boldsymbol{\delta}_i$ and $\boldsymbol{\delta}_{i,m}$ are unit spikes at samples i and $i + m$, respectively. The even (+) and odd (−) dipoles represent layers bounded by reflection coefficients of the same and opposite polarities, respectively. $m_{\max}$ is the maximum dipole thickness in samples and is set to half the period of the analysis wavelet, i.e., $m_{\max} = \mathrm{round}[1/(2kf_{ad}\Delta t)]$. Hence, $\mathbf{A}_{MM} = \mathbf{WD}$ has $N \times N(2m_{\max} + 1)$ entries ($400 \times 14{,}800$ for the synthetic traces in Section 3.1, with $m_{\max} = 18$), where $\mathbf{D}$ is the wedge (dipole) synthesis matrix. In practice, $\mathbf{A}_{MM}$ is never formed explicitly but is applied by fast convolution. The columns are not normalized, so the ℓ_1 norm acts on the amplitude of each spike or dipole. This weighting favors representing a thin layer by one dipole rather

than by two independent spikes. To preserve the relative amplitudes between traces, all traces are scaled by a single global factor s (the 99.9th percentile of the absolute amplitude of the volume), $\tilde{\mathbf{d}} = \mathbf{d}/s$, and the output is rescaled by s. Equation (4) is solved trace by trace with the fast iterative shrinkage-thresholding algorithm (FISTA) [70], using the step size $1/L$, where $L = \|\mathbf{A}_{MM}\|_2{}^2$ is estimated by power iteration. The iterations stop when the relative change in $\mathbf{x}$ is less than 10^{-4} or after 200 iterations. The regularization parameter is set as $\lambda = \lambda_r \|\mathbf{A}_{MM}{}^{\mathrm{T}}\tilde{\mathbf{d}}\|_\infty$, where the relative regularization parameter λ_r is selected by the discrepancy principle described in Section 2.6. The sparse reflectivity estimate, which consists of the single spikes and dipoles selected by BPDN, is

$$\hat{\mathbf{r}} = \mathbf{D}\hat{\mathbf{x}} \tag{6}$$

An appropriate compression coefficient is selected to compress $\omega(t)$ along the time axis to generate the high-frequency synthetic analysis wavelet sequence $\omega(\beta t)$. The corresponding expression is given in Equation (7).

$$\omega(\beta t) = \frac{1}{\sqrt{2\pi}\sigma}\exp\left(-\frac{\beta^2 t^2}{2\sigma^2}\right)\exp(j2\pi\beta k f_{ad} t) \tag{7}$$

where β is the wavelet compression coefficient, whose value affects the high-resolution processing result. In general, β should not be excessively large; otherwise, the reliability of some frequency components may be reduced. Time compression by β scales the spectrum of the wavelet: the center frequency and the absolute bandwidth increase by a factor of β, whereas the relative bandwidth and the zero phase are preserved. Therefore, BPFE shifts and broadens the effective band toward higher frequencies but does not add low-frequency components below the original band. The same zero-mean correction and unit-peak normalization are applied to the real part of $\omega(\beta t)$, so that an isolated reflector keeps its amplitude after processing. An objective rule for selecting β is given in Section 2.6.

The sparse representation obtained on the low-frequency analysis-specific wavelet sequence is combined with the high-frequency synthetic analysis wavelet sequence to reconstruct the seismic record, thereby generating the high-resolution seismic data $y(t)$:

$$y(t) = \omega(\beta t) * r(t) \tag{8}$$

where $*$ denotes the convolution operation and $r(t)$ is the sparse reflectivity estimate $\hat{\mathbf{r}}$ of Equation (6).

The BPDN algorithm is a classical and widely used convex optimization reconstruction algorithm in compressed sensing and sparse signal processing [67–69]. It has been applied to seismic random noise suppression [71] and seismic reflectivity inversion debiasing [72]. The BPDN algorithm uses the sparsity of signals under a specific basis or dictionary to solve the problem of sparse signal reconstruction under noise interference. In practical applications, observed signals are inevitably contaminated by noise. Therefore, equality constraints under noise-free conditions are no longer applicable, and noise tolerance must be introduced to balance reconstruction accuracy and signal sparsity. Unlike basis pursuit, BPDN considers the possible presence of noise in the signal in the model and aims to remove the influence of noise as much as possible during sparse representation, which is of considerable practical significance. Because of the ℓ_1 penalty, BPDN shrinks small coefficients toward zero; λ therefore controls the trade-off between noise suppression and the preservation of weak reflections.

2.2. Formation Dip and Azimuth Extraction Using the Gradient Structure Tensor

The gradient structure tensor algorithm constructs a structure tensor from the gradient vectors of seismic amplitudes to calculate formation dip and azimuth attributes [73,74]. It can effectively describe structural features in seismic data. Formation dip and azimuth are basic geological concepts and important components of seismic geometric attributes, and they also play an important role in seismic processing and interpretation [32,75]. As important seismic structural attributes, dip and azimuth not only reveal the inclination of subsurface rock formations and identify faults but also provide the basis for extracting many other seismic attributes. If the derived dip and azimuth attributes are inaccurate or incomplete, the corresponding seismic geometric attributes will also be affected, and their performance may be lower than expected.

The calculation steps for the gradient structure tensor of 3D seismic data are as follows [32,35]. First, the gradient vector $\nabla u(x, y, z)$ at each point in the seismic data volume is calculated as follows:

$$\boldsymbol{g} = \nabla u(x,y,z) = \begin{bmatrix} \frac{\partial u(x,y,z)}{\partial x} \\ \frac{\partial u(x,y,z)}{\partial y} \\ \frac{\partial u(x,y,z)}{\partial z} \end{bmatrix} = \begin{bmatrix} g_x \\ g_y \\ g_z \end{bmatrix} \tag{9}$$

where $g_x = \partial u(x, y, z)/\partial x$, $g_y = \partial u(x, y, z)/\partial y$, and $g_z = \partial u(x, y, z)/\partial z$ are the components of the gradient vector along the x, y, and z directions, respectively.

Then, the gradient structure tensor is constructed at each position from the computed gradient vectors:

$$\boldsymbol{T} = \begin{bmatrix} T_{11} & T_{12} & T_{13} \\ T_{21} & T_{22} & T_{23} \\ T_{31} & T_{32} & T_{33} \end{bmatrix} = \boldsymbol{g}\boldsymbol{g}^T = \begin{bmatrix} g_x^2 & g_x g_y & g_x g_z \\ g_y g_x & g_y^2 & g_y g_z \\ g_z g_x & g_z g_y & g_z^2 \end{bmatrix} \tag{10}$$

$\boldsymbol{T}$ is then expressed using eigenvalues and eigenvectors as follows:

$$\boldsymbol{T} = \begin{pmatrix} v_1 & v_2 & v_3 \end{pmatrix} \begin{bmatrix} \lambda_1 & 0 & 0 \\ 0 & \lambda_2 & 0 \\ 0 & 0 & \lambda_3 \end{bmatrix} \begin{pmatrix} v_1 & v_2 & v_3 \end{pmatrix}^T \tag{11}$$

where λ_1, λ_2, and λ_3 are the eigenvalues of $\boldsymbol{T}$ and satisfy $\lambda_1 \geq \lambda_2 \geq \lambda_3 \geq 0$; v_1, v_2, and v_3 are the eigenvectors corresponding to λ_1, λ_2, and λ_3, respectively. Here, λ_1 is the principal eigenvalue, and v_1 is the principal eigenvector. The latter indicates the dominant gradient direction of the signal, which is normal to the local reflector (formation normal). v_2 and v_3 span the local plane parallel to the reflector, i.e., perpendicular to v_1. In practice, each element of $\boldsymbol{T}$ is smoothed with a Gaussian window before the eigendecomposition to stabilize the estimate [73].

Ultimately, using v_1, the dip and azimuth can be defined as follows:

$$\theta = \arctan[\sqrt{v_1^2(x) + v_1^2(y)}/|v_1(z)|] \tag{12}$$

$$\varphi = \arctan[v_1(y)/v_1(x)] \tag{13}$$

where $v_1(x)$, $v_1(y)$ and $v_1(z)$ are the components of v_1 along the x, y and z directions, respectively. Here, θ is the dip angle measured from the horizontal plane, so horizontal layers (v_1 parallel to the z axis) have zero dip, and φ is the dip azimuth computed with the four-quadrant arctangent.

2.3. Coherence Attribute Calculation

Seismic coherence analysis evaluates the waveform similarity between each sampling point and its neighboring data in a seismic volume, converting amplitude characteristics into a coherence volume to describe discontinuities in subsurface strata [38–41]. Ideally, seismic discontinuities represent geological discontinuities [39], and high coherence values indicate no obvious stratigraphic or structural changes in the area. When seismic traces are cut by a fault plane, their responses usually differ from those of adjacent traces, resulting in abnormal coherence among local traces. Therefore, low coherence values indicate seismic discontinuities. Eigenvalue coherence is obtained from the eigenvalues of the covariance matrix of the seismic data. For a seismic data volume, N sampling points from J adjacent traces are selected to form an $N \times J$ data matrix.

$$\boldsymbol{D} = \begin{bmatrix} d_{11} & d_{12} & \dots & d_{1J} \\ d_{21} & d_{22} & \dots & d_{2J} \\ \vdots & \vdots & \ddots & \vdots \\ d_{N1} & d_{N2} & \dots & d_{NJ} \end{bmatrix} \tag{14}$$

Then, the covariance matrix of the seismic data volume can be expressed as

$$\boldsymbol{C} = \boldsymbol{D}^T\boldsymbol{D} = \sum_{n=1}^{N} \boldsymbol{d}_n \boldsymbol{d}_n^T = \begin{bmatrix} \sum_{n=1}^{N} d_{n1}d_{n1} & \sum_{n=1}^{N} d_{n1}d_{n2} & \dots & \sum_{n=1}^{N} d_{n1}d_{nJ} \\ \sum_{n=1}^{N} d_{n2}d_{n1} & \sum_{n=1}^{N} d_{n2}d_{n2} & \dots & \sum_{n=1}^{N} d_{n2}d_{nJ} \\ \vdots & \vdots & \ddots & \vdots \\ \sum_{n=1}^{N} d_{nJ}d_{n1} & \sum_{n=1}^{N} d_{nJ}d_{n2} & \dots & \sum_{n=1}^{N} d_{nJ}d_{nJ} \end{bmatrix} \tag{15}$$

According to Equation (15), the third-generation coherence algorithm can be expressed as

$$C_3 = \lambda_{\max} / \sum_{j}^{J} \lambda_j \tag{16}$$

where $\lambda_{\max}$ is the largest eigenvalue, and λ_j represents the j-th eigenvalue.

The sum of the eigenvalues of the covariance matrix equals the sum of its diagonal elements:

$$Tr(C) = \sum_{j=1}^{J} \sum_{n=1}^{N} d_{nj}^2 = \sum_{j=1}^{J} \lambda_j \tag{17}$$

The final expression of the third-generation coherence algorithm is

$$C_3 = \lambda_{\max} / Tr(C) \tag{18}$$

where $Tr(C) \geq 0$ is the trace of the covariance matrix. When the covariance matrix is large, calculating coherence using the matrix trace is more efficient than summing the eigenvalues.

2.4. Ant-Tracking Attribute Calculation

As a relatively mature technique for enhancing fractures and faults in complex seismic data, ant tracking can characterize their development and distribution more accurately and objectively. In the seismic data volume, a large number of initial ants are deployed to search for possible fault and fracture surfaces along random paths. These ants release pheromones, which attract subsequent ants within a certain range to jointly track discontinuities. The ants preferentially follow paths with higher pheromone concentrations, thereby delineating discontinuities in the seismic data and identifying faults and fractures [45–48]. In contrast, other paths with a low probability of being detected as faults and fractures are gradually abandoned by the ants because of pheromone evaporation. The final optimal foraging

paths are regarded as the detected faults and fractures. Compared with other seismic attributes used for fault and fracture identification, ant-tracking attributes have lower noise and provide clearer fracture characterization. Moreover, during tracking, search parameters can be adjusted according to geological interpretation results, thereby enabling the identification of fractures with different orientations [35,41].

The ant-tracking algorithm primarily involves two processes: state transition and pheromone update. Given an ant colony of size m and a network of n nodes, the ant colony algorithm flow from [76] is presented in Figure 2. Note that the ant-tracking volumes in this study were computed using Petrel. Equations (19)–(21) and Figure 2 describe the underlying ant colony optimization principle.

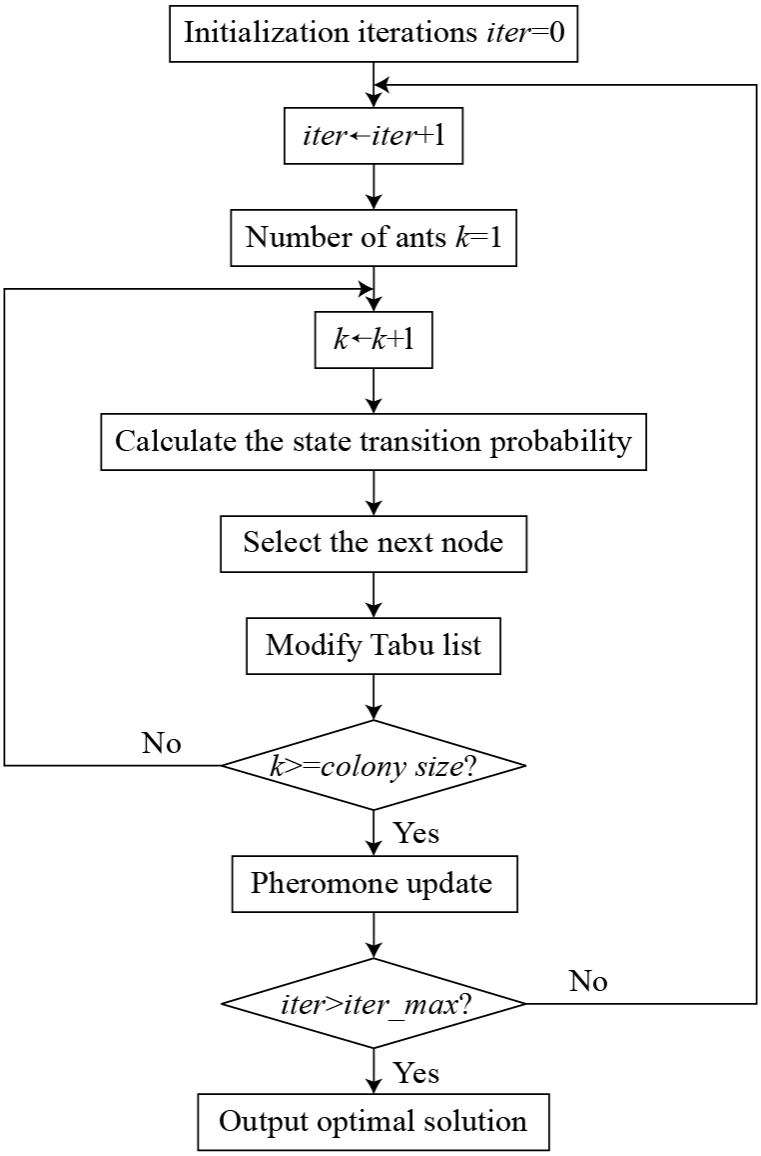


Figure 2. Ant colony tracking algorithm flowchart [76].

State transition. At time t, the ants randomly select the next node. The probability $p_{ij}{}^{k}(t)$ that ant k at node i selects node j as the transition target is calculated as:

$$p_{ij}^{k}(t) = \begin{cases} \frac{\tau_{ij}^{\alpha}(t)\eta_{ij}^{\mu}(t)}{\sum_{s \in allow_k} \tau_{is}^{\alpha}(t)\eta_{is}^{\mu}(t)}, & j \in allow_k \\ 0, & j \notin allow_k \end{cases} \quad (19)$$

where $\tau_{ij}(t)$ represents the pheromone concentration on path (i, j) at time t, and $\eta_{ij}(t)$ denotes the heuristic information of path (i, j), which is usually taken as the reciprocal of the arc distance d_{ij}. The pheromone heuristic factor α indicates the importance of pheromones and reflects the degree of ant collaboration, whereas the expected heuristic factor μ represents the importance of heuristic information. The set $allow_k$ contains the nodes not yet visited by ant k at time t and is commonly maintained using a tabu list.

Pheromone update. Excessive pheromone accumulation may overly strengthen the pheromone heuristic effect and overwhelm the expected heuristic effect. To prevent this, pheromone accumulation and evaporation are performed on each path after each ant completes one iteration. The formulas for updating pheromones on path (i, j) at time $t + n$ are

$$\tau_{ij}(t + n) = (1 - \rho)\tau_{ij}(t) + \Delta\tau_{ij}(t) \quad (20)$$

$$\Delta\tau_{ij}(t) = \sum_{k=1}^{m} \Delta\tau_{ij}^{k}(t) \quad (21)$$

where ρ is the pheromone evaporation factor, $(1 - \rho)\tau_{ij}(t)$ is the pheromone remaining after evaporation, $\Delta\tau_{ij}(t)$ is the pheromone increment at time t, and m is the ant colony size. As pheromones accumulate on the paths during the ant search process, the pheromone concentration is continuously updated and adjusted in each iteration.

2.5. Multiscale Fracture Prediction Integrating BPFE with Multi-Attribute Fusion

The workflow of the multiscale fracture prediction method integrating BPFE with multi-attribute fusion is shown in Figure 3. First, BPFE-based high-resolution processing is performed on the seismic data using the BPDN algorithm in compressed sensing. This step enhances the high-frequency energy of seismic signals and improves the ability to identify small-scale fractures. Then, the gradient structure tensor algorithm is used to extract formation dip and azimuth information. On this basis, the third-generation eigenvalue coherence algorithm and ant-tracking technology are used to calculate coherence and ant-tracking attributes, which characterize fracture development and distribution at different scales. Finally, the small-scale fracture probability obtained from ant tracking is fused with the large-scale fault and fracture probability derived from coherence analysis to yield a complete multiscale fault and fracture system. The specific steps are as follows:

BPFE-based high-resolution seismic processing. First, the average dominant frequency of the seismic data is estimated using the Fourier transform and is used to generate a low-frequency analysis-specific wavelet sequence. Then, the sparse representation of the original seismic data on this wavelet sequence is reconstructed using BPDN. On this basis, an appropriate wavelet compression coefficient is selected to generate the high-frequency synthetic analysis wavelet sequence. Finally, this synthetic wavelet sequence and the sparse representation are used to reconstruct seismic records with high-frequency wavelets, thereby generating high-resolution data.

Formation dip and azimuth extraction. First, the gradient vector is calculated at each sampling point of the 3D seismic data volume. The resulting gradient vectors are then used to construct the gradient structure tensor. Finally, eigendecomposition is performed on the gradient structure tensor. The eigenvector v_1 corresponding to the largest eigenvalue is taken as the formation normal, from which the formation dip and azimuth are derived (Equations (12) and (13)).

Coherence and ant-tracking attribute calculation. The third-generation eigenvalue coherence algorithm is used to extract seismic coherence attributes. Dip-guided volume control is applied to reduce the influence of formation dip on the coherence values between seismic traces. Meanwhile, a 3D variance volume is calculated from the seismic data. The

ant-tracking algorithm is then applied to the variance volume to track faults and fractures, yielding the ant-tracking attributes.

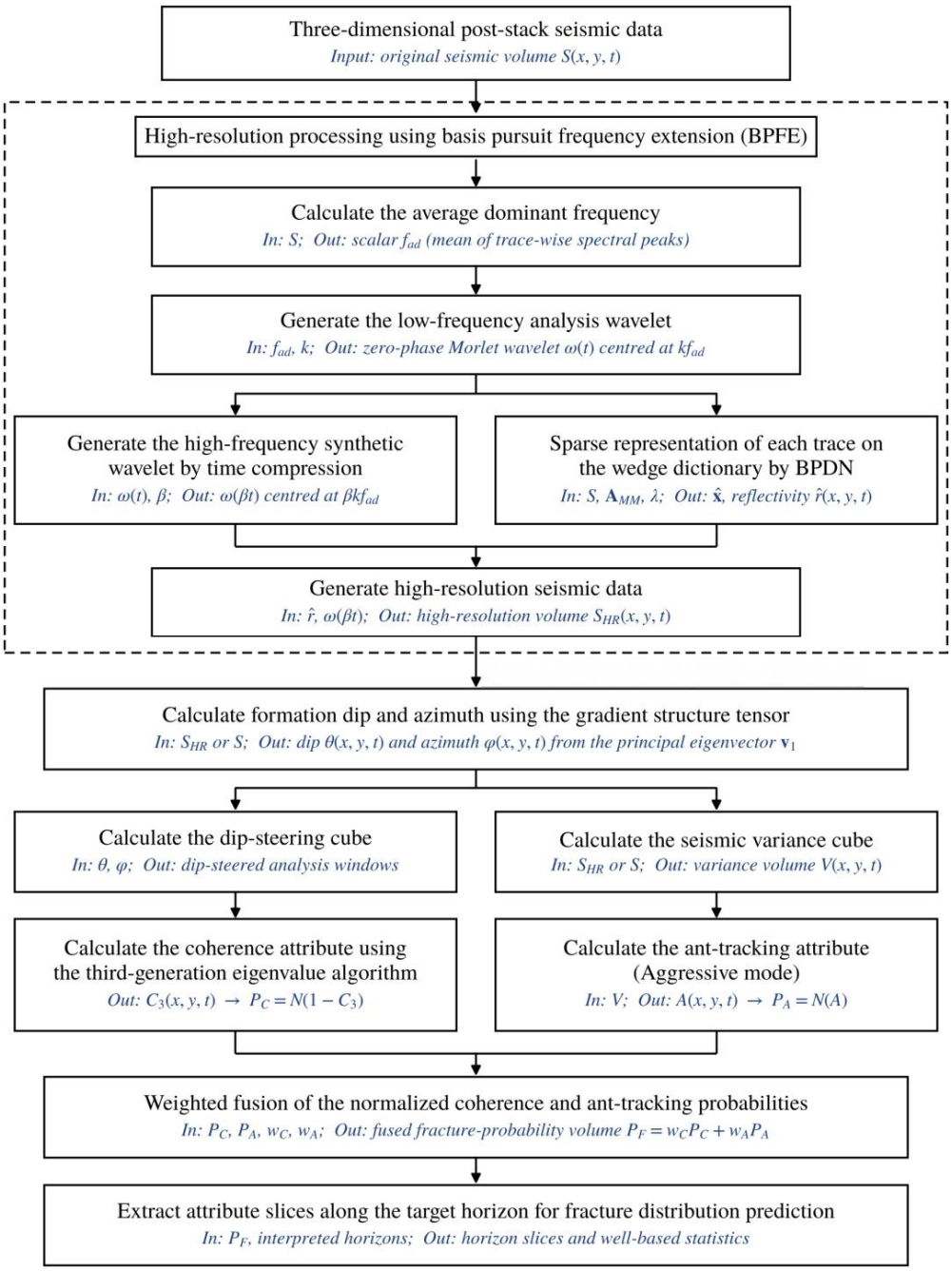


Figure 3. Workflow of the multiscale fracture prediction method integrating basis pursuit frequency extension and multi-attribute fusion. The dashed box encloses the BPFE-based high-resolution processing steps, and the arrows indicate the processing sequence and data flow. The input (In) and output (Out) data volumes of each step are annotated in italics.

Coherence and ant-tracking attribute fusion. The two attributes have different physical meanings, ranges and polarities (low coherence and high ant-tracking values indicate discontinuities). Therefore, they are first converted into dimensionless fracture-probability volumes in the range of 0–1 by a robust min–max normalization computed over the target interval:

$$N(a) = \min\left\{1, \max\left[0, \frac{a - a_{p1}}{a_{p99} - a_{p1}}\right]\right\} \tag{22}$$

where a_{p1} and a_{p99} are the 1st and 99th percentiles of attribute a within the target interval, which suppresses the influence of outliers and removes the dimensional differences between the attributes. The coherence-derived (large-scale) probability is $P_C = N(1 - C_3)$, and the ant-tracking-derived (small-scale) probability is $P_A = N(A)$, where A is the ant-tracking attribute. The two volumes are then fused by a weighted sum:

$$P_F(x, y, t) = w_C P_C(x, y, t) + w_A P_A(x, y, t),\ w_C + w_A = 1 \tag{23}$$

where w_C and w_A are spatially constant weights. The weights express the complementary attribute-sensitive scales: coherence retains the main faults and laterally continuous discontinuities, whereas ant tracking supplies laterally short and weak discontinuities. For interpretation, the attribute-sensitive scale classes are defined operationally from the normalized volumes using a threshold of $\xi = 0.5$. Large-scale discontinuities are clearly expressed in coherence ($P_C \geq \xi$). Medium-scale discontinuities are weakly expressed in coherence but enhanced by ant tracking ($\xi/2 \leq P_C < \xi$ and $P_A \geq \xi$). Small-scale discontinuities are detected by ant tracking only ($P_C < \xi/2$ and $P_A \geq \xi$). These classes refer to seismic-attribute scales, not to the physical aperture or length of individual fractures. The same normalization, weights and display scale are used for the fusion results with and without BPFE.

Multiscale fracture distribution prediction. Based on the fused multiscale fracture probability volume, attributes are extracted along the target interval to predict fracture development and distribution. The prediction results are compared with those obtained from coherence and ant-tracking attributes, and further analysis and evaluation are performed in combination with geological and well-log interpretation results.

2.6. Parameter Selection Rules and Evaluation Metrics

To make the processing reproducible, the three BPFE parameters are selected using the following objective rules, which rely only on the seismic data themselves. The rules were verified with the synthetic data, and the parameters used in this study are listed in Table 1.

Table 1. Processing parameters and settings used in this study.

Step	Parameters	Settings
BPFE	Adjustment factor k (rule (1))	1.20
	Relative bandwidth γ of the Morlet wavelet	0.45
	Compression coefficient β (rule (3))	1.50
	Relative regularization λ_r (rule (2))	0.002 (noise-free) to 0.02 (0 dB)
	Maximum dipole thickness $m_{\max}$ (samples)	18
	Solver and stopping criterion	FISTA; $\leq$200 iterations; 10^{-4}
	Amplitude normalization	Global, 99.9th percentile
Coherence	Window (J traces $\times$ N samples)	3 traces $\times$ 17 samples
Ant tracking	Initial ant boundary/ant track deviation/ant step size/illegal steps allowed/legal steps required/search threshold	5/2/3/2/2/10
Fusion	Normalization (Equation (22))	1st–99th percentiles
	Scale-class threshold ξ (large/medium/small)	0.50

Adjustment factor k. For each candidate $k \in [1.0, 2.0]$ (step 0.05), the correlation coefficient is computed between the amplitude spectrum $|W(f)|$ of the analysis wavelet and the average amplitude spectrum of the data smoothed over 10 Hz. The value of k that maximizes this correlation is selected. This one-parameter spectral match uses

only the shape of the amplitude spectrum and does not require wavelet extraction or a phase estimate.

Regularization parameter λ. Following the discrepancy principle, λ_r is chosen on the logarithmic grid $\{0.002, 0.005, 0.01, 0.02, 0.05, 0.1, 0.2\}$ as the largest value whose relative data residual $\|\widetilde{\mathbf{d}} - \mathbf{A}_{MM}\hat{\mathbf{x}}\|_2 / \|\widetilde{\mathbf{d}}\|_2$ does not exceed $\max(0.85\hat{\varepsilon}, 0.04)$. Here, $\hat{\varepsilon}$ is the noise-to-data root-mean-square (RMS) ratio estimated from the average power spectrum beyond the signal band (assuming approximately white noise within the recording band), and 0.04 is a floor that accounts for the approximation error of the analysis wavelet. The factor 0.85 was calibrated with the synthetic data.

Compression coefficient β. β controls the trade-off between resolution and reliability. It is selected as the largest value not exceeding 1.6 for which the median coherence of the processed data within the target interval does not decrease by more than 5% relative to $\beta = 1$ (i.e., the same sparse reconstruction without compression). A larger decrease indicates that the extended band is dominated by noise or reconstruction artifacts, which would create spurious discontinuities. The upper bound of 1.6 is the largest value for which the synthetic tests on noise-free data gave a correlation coefficient above 0.95 with the ideal reference and a spurious-event rate below 7%.

The following metrics are used to quantify the results. The dominant frequency f_d is the peak frequency of the average amplitude spectrum smoothed with a 20 Hz running window, and the effective bandwidth is the -6 dB (half-amplitude) band $[f_L, f_H]$ of the same spectrum. The vertical resolution is expressed by the quarter-wavelength (Rayleigh) criterion $\Delta z = v/(4f_d)$, where v is the interval velocity. For the synthetic wedge model, it is also expressed by the tuning thickness, i.e., the thickness at which the composite peak-to-trough amplitude reaches its maximum [77,78]. Reconstruction fidelity is measured by the correlation coefficient (CC) and by the reconstruction signal-to-noise ratio (SNR), $\mathrm{SNR}_r = 10\log_{10}(\|\mathbf{y}_{\mathrm{ref}}\|^2 / \|\mathbf{y}_{\mathrm{ref}} - s\mathbf{y}\|^2)$, between the output $\mathbf{y}$ and the ideal reference $\mathbf{y}_{\mathrm{ref}}$, where s is a least-squares scale factor. Phase fidelity is measured by the mean and the amplitude-weighted RMS phase difference between $\mathbf{y}$ and $\mathbf{y}_{\mathrm{ref}}$ within the band in which the reference amplitude exceeds 10% of its maximum. Relative amplitude preservation is measured by the mean relative error of the trace-averaged amplitudes of five isolated key reflectors after a single least-squares scaling. Spurious events are output extrema with amplitudes larger than 10% of the reference maximum that have no extremum of the same polarity in the reference within ± 2 ms. Discontinuity detection is evaluated using the third-generation coherence C_3 in terms of two measures. The first is the area under the receiver operating characteristic curve (AUC) [79] between discontinuity and background samples. The second is the minimum detectable throw, i.e., the smallest throw above which all discontinuities show a mean $1 - C_3$ exceeding the background mean by more than three standard deviations.

3. Results

3.1. Synthetic Data Tests

3.1.1. Synthetic Model and Test Design

A two-dimensional synthetic model with known reflectivity was designed to quantify the fidelity, noise robustness and parameter sensitivity of BPFE and to compare it with conventional resolution-enhancement methods (Figure 4). The model contains 180 traces with 400 samples (sample interval 1 ms). It includes five isolated key reflectors used to check amplitude preservation, four packages of thin sand–mud interbeds with thicknesses of 3–12 ms and weak random background reflectivity. The model also includes gentle folding (± 3 ms), smooth lateral amplitude variations ($\pm 10\%$) and seven vertical faults with throws of 1, 2, 3, 4, 5, 6 and 8 ms. In addition, it contains seven bed-confined local discontinuities

(fracture zones), in which a single thin bed (3–11 ms thick) is offset by 0.5–6 ms over three traces while the surrounding layers remain continuous. The bed-confined zones mimic small-scale fractures with weak seismic responses, whose signature is a subtle waveform change within a thin layer. The seismic data were computed in the frequency domain with a zero-phase 25 Hz Ricker wavelet. A wedge model (top reflection coefficient +0.1, base −0.1, thickness 0–40 ms) was also appended to evaluate thin-bed resolution. Band-limited (5–120 Hz) Gaussian noise was added at SNRs of 20, 10, 5 and 0 dB, where SNR = $10\log_{10}(P_s/P_n)$, and P_s and P_n are the signal and noise powers, respectively. To test the stationarity assumption, a second dataset was generated with constant-Q attenuation (Q = 60) within the 400 ms window.

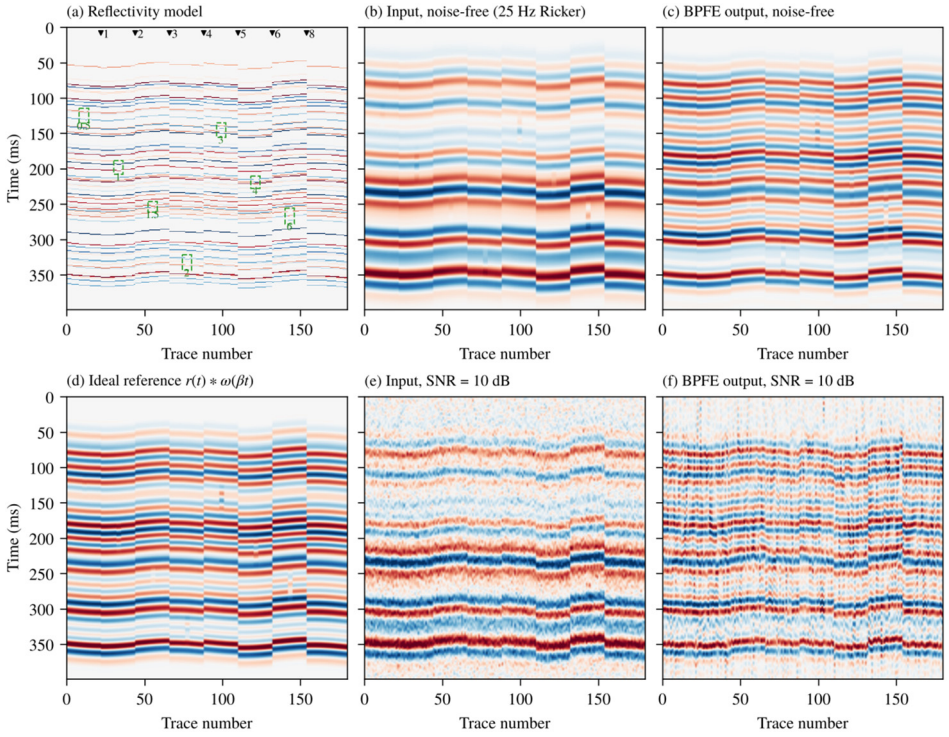


Figure 4. Synthetic model and BPFE results: (**a**) reflectivity model; black triangles mark the faults and green dashed boxes mark the bed-confined local discontinuities (throws in ms); (**b**) noise-free input computed with a 25 Hz Ricker wavelet; (**c**) BPFE output (k = 1.20, β = 1.5, λ_r = 0.002); (**d**) ideal reference $r(t) * \omega(\beta t)$, where $*$ denotes convolution; (**e**) input with SNR = 10 dB; (**f**) BPFE output of (**e**) (λ_r = 0.005 selected by rule (2)). Panels (**c**,**d**,**f**) use the same color scale. In all panels, red and blue denote positive and negative values (reflection coefficients or amplitudes), respectively.

Because BPFE outputs a band-limited seismic record rather than a reflectivity series, its ideal output is the true reflectivity convolved with the synthesis wavelet, $r(t) * \omega(\beta t)$ (Figure 4d), which is used as the reference for all fidelity metrics. For the comparison in Section 3.1.5, all methods except inverse-Q filtering were shaped to the same target amplitude spectrum $|W(f/\beta)|$ so that they aim at the same reference. The average dominant frequency of the noise-free data was f_{ad} = 22.9 Hz, and rule (1) gave k = 1.20 (analysis wavelet centered at 27.5 Hz), β = 1.5 was used unless otherwise stated (synthesis wavelet centered at 41.3 Hz), and $m_{\max}$ = 18 samples. For reproducibility, the parameters are listed in Table 1 and the BPFE algorithm is summarized in Algorithm 1.

Algorithm 1. Basis pursuit frequency extension (BPFE)

Input: seismic volume $\mathbf{S}$ (M traces $\times$ N samples), sample interval Δt, relative bandwidth γ, candidate grids for k, λ_r and β.

Output: high-resolution volume $\mathbf{S}_{\mathrm{HR}}$.

1: $f_{ad} \leftarrow$ mean over traces of $\arg\max_f |fft(x_i)|$ (Equation (1)).

2: $k \leftarrow \arg\max_k \mathrm{corr}(|W(f; kf_{ad})|$, smoothed mean amplitude spectrum of $\mathbf{S})$ (rule (1)).
3: $\sigma \leftarrow 1/(2\pi\gamma k f_{ad})$; $w_a(t) \leftarrow \mathrm{Re}\{\omega(t)\}$ (Equation (2)), zero-mean, unit peak; $m_{\max} \leftarrow \mathrm{round}[1/(2kf_{ad}\Delta t)]$.

4: Build the operator $\mathbf{A}_{MM} = \mathbf{WD}$ (single spikes, even and odd dipoles, $m = 1, \ldots, m_{\max}$; Equation (5)).

5: $s \leftarrow$ 99.9th percentile of $\left|\mathbf{S}\right|$; $\widetilde{\mathbf{D}} \leftarrow \mathbf{S}/s$; $\hat{\varepsilon} \leftarrow$ noise-to-data RMS ratio from the spectral tail.

6: **for** λ_r in the grid (ascending) **do**

7: $\lambda \leftarrow \lambda_r \|\mathbf{A}_{MM}{}^{\mathrm{T}}\widetilde{\mathbf{D}}\|_\infty$; solve Equation (4) for every trace by FISTA (step $1/L$, $\leq$200 iterations, tolerance 10^{-4}).

8 : **if** $\|\widetilde{\mathbf{D}} - \mathbf{A}_{MM}\hat{\mathbf{X}}\| / \|\widetilde{\mathbf{D}}\| > \max(0.85\hat{\varepsilon}, 0.04)$ **then break**; **else** keep $\hat{\mathbf{X}}$ (rule (2)).

9 : $\hat{\mathbf{R}} \leftarrow \mathbf{D}\hat{\mathbf{X}}$ (Equation (6)).

10: **for** β in the grid (ascending, $\leq$1.6) **do** $\mathbf{S}_\beta \leftarrow s \cdot (\hat{\mathbf{R}} * \mathrm{Re}\{\omega(\beta t)\})$ (Equations (7) and (8)); keep the largest β whose median coherence decreases by $\leq$5% relative to $\beta = 1$ (rule (3)).

11: **return** $\mathbf{S}_{\mathrm{HR}} = \mathbf{S}_\beta$.

3.1.2. Fidelity with Known Reflectivity

For noise-free data, the BPFE output reproduces the ideal reference with CC = 0.978 and SNR_r = 13.6 dB (Figure 4c,d). The dominant frequency increases from 30.8 to 49.3 Hz (reference: 49.8 Hz), and the -6 dB band changes from 12.7–43.5 Hz to 23.9–59.6 Hz (reference: 26.9–62.0 Hz; Figure 5a); i.e., the upper band limit increases by 37% and the absolute bandwidth by 16%, whereas the lower band limit also moves upward, consistent with the spectral scaling by β. With an interval velocity of 4000 m/s, the quarter-wavelength resolution improves from 32.5 to 20.3 m. The mean phase difference between the output and the reference is -0.7°; i.e., no systematic phase rotation is introduced. Nevertheless, frequency-dependent deviations with an RMS value of 24° occur, mainly near the band edges where the amplitudes are low (Figure 5b). The relative amplitudes of the key reflectors are preserved with a mean error of 11.8%, which is mainly caused by the ℓ_1 shrinkage of weak events. The trace comparison in Figure 5c shows that the BPFE output closely follows the reference. Only 2.5% of the output extrema are spurious, and 16.0% of the energy of the sparse reflectivity $\hat{\mathbf{r}}$ lies farther than 2 ms from the true reflectors. This indicates that the sparse prior introduces weak side events but no strong spurious reflections.

For the wedge model (Figure 5d), the tuning thickness decreases from 16 ms for the input to 11 ms after BPFE (reference: 10 ms). Moreover, the mean absolute error of the apparent thickness for beds of 8–14 ms decreases from 3.4 to 1.4 ms. For thicker beds ($\geq$15 ms), the apparent thickness after BPFE deviates from the true thickness by 0.4 ms on average. This deviation corresponds to sub-sample timing jitter caused by approximating the Ricker wavelet with the Morlet analysis wavelet. These results show that BPFE improves

the vertical resolution by approximately one-third without introducing systematic time shifts or phase rotations.

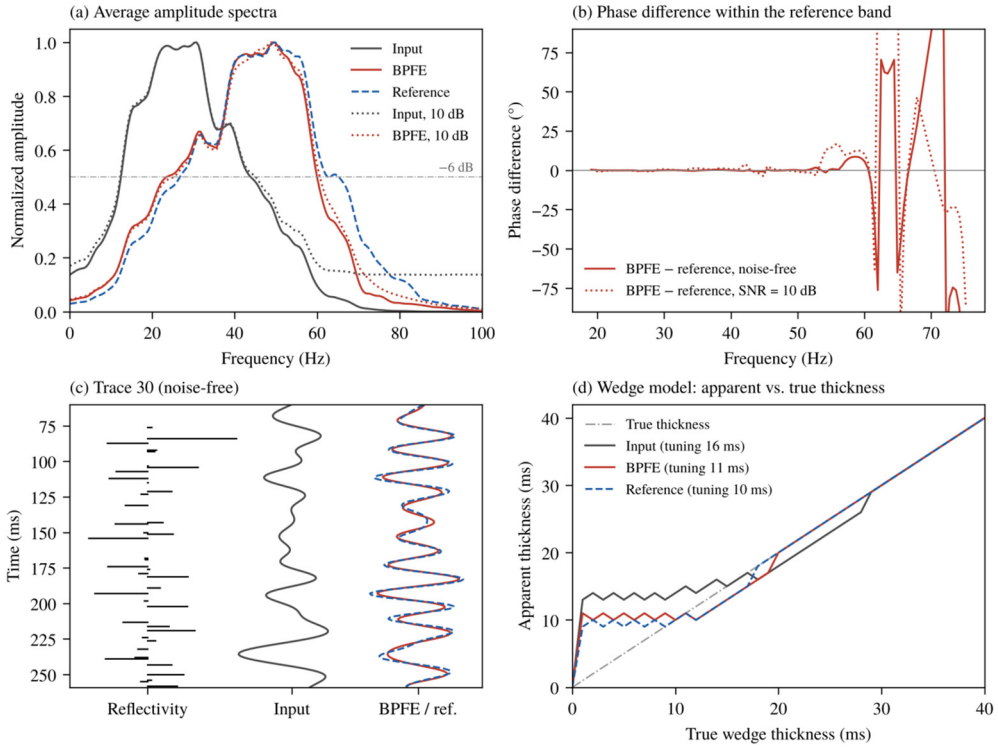


Figure 5. Fidelity of BPFE for the synthetic data: (**a**) average amplitude spectra (20 Hz smoothing) of the input, BPFE output and ideal reference for noise-free data and SNR = 10 dB; (**b**) phase difference between the BPFE output and the reference within the reference band; (**c**) comparison of trace 30 (solid: BPFE; dashed: reference) with the true reflectivity; (**d**) apparent versus true thickness for the wedge model.

3.1.3. Noise Robustness and Detectability of Small-Scale Discontinuities

Table 2 and Figure 6 summarize the results for SNRs from ∞ to 0 dB, with λ_r selected by rule (2). The CC between the BPFE output and the noise-free reference decreases from 0.978 (noise-free) to 0.964, 0.882, 0.786 and 0.647 at 20, 10, 5 and 0 dB, respectively. This decrease shows that frequency extension inevitably transfers part of the noise into the extended band. However, the BPFE output contains fewer spurious events than the noisy input itself (23.4% versus 48.4% at 10 dB; Figure 6c), because BPDN suppresses noise that cannot be sparsely represented by the dictionary. In addition, the mean phase difference remains within $\pm 11^\circ$ at all noise levels.

Table 2. Performance of BPFE for the synthetic data at different noise levels.

SNR (dB)	λ_r	CC	SNR_r (dB)	Mean/RMS Phase (°)	Spurious Events (%)	Fault AUC	Local-Zone AUC
∞	0.002	0.978	13.6	−0.7/24.0	2.5	0.987 → 1.000	0.951 → 0.946
20	0.002	0.964	11.5	−0.8/24.8	6.3	0.903 → 0.925	0.715 → 0.794
10	0.005	0.882	6.5	4.5/26.2	23.4	0.740 → 0.769	0.580 → 0.687
5	0.01	0.786	4.2	9.1/30.1	36.6	0.652 → 0.680	0.537 → 0.623
0	0.02	0.647	2.4	10.9/31.9	48.6	0.588 → 0.592	0.479 → 0.542

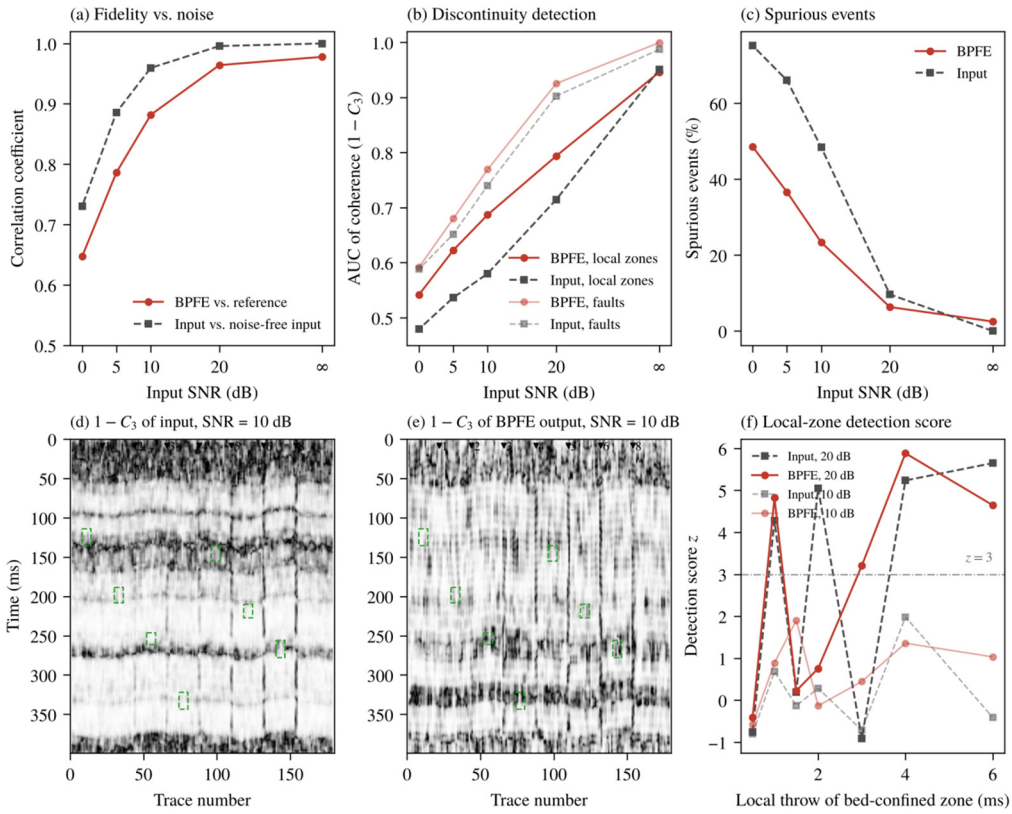


Figure 6. Noise robustness and discontinuity detection for the synthetic data: (**a**) CC of the BPFE output with the noise-free reference and CC of the noisy input with the noise-free input; (**b**) AUC of the coherence attribute for the faults and the bed-confined local zones; (**c**) percentage of spurious events; (**d**,**e**) coherence discontinuity $1 - C_3$ of the input and BPFE output at SNR = 10 dB (triangles: faults; dashed boxes: local zones); (**f**) detection score z of the local zones versus local throw.

The coherence-based detection results (Figure 6b,d–f) show that BPFE mainly improves the detectability of the bed-confined local discontinuities, whose responses are weak and confined to thin layers. For these discontinuities, the AUC increases from 0.715 to 0.794 at 20 dB, from 0.580 to 0.687 at 10 dB and from 0.537 to 0.623 at 5 dB. In addition, the minimum detectable local throw at 20 dB decreases from 4 to 3 ms. For the through-going faults, the AUC increases only slightly (from 0.903 to 0.925 at 20 dB and from 0.740 to 0.769 at 10 dB). The minimum detectable fault throw remains unchanged at 20 dB (2 ms) and increases slightly at 10 dB (from 2 to 3 ms). At 0 dB, the fault AUC is almost unchanged (0.588 versus 0.592), and the minimum detectable fault throw increases from 5 to 8 ms. The detection score of individual zones also depends on the thickness of the offset bed and its interference with neighboring reflectors (Figure 6f). Therefore, BPFE is most beneficial for weak, vertically confined discontinuities in thin interbeds (the targets of this study), and its benefit decreases as the SNR decreases. In terms of physical scale, a throw of 3 ms corresponds to approximately 6 m at 4000 m/s. Hence, the detectable discontinuities are seismic-scale offsets or fracture zones that modify the waveform, rather than individual fractures with millimeter- to centimeter-scale apertures.

3.1.4. Parameter Sensitivity and Selection

Figure 7 shows the sensitivity of BPFE to k, λ and β. To isolate the effect of k, the sparse reflectivity obtained with each k was re-synthesized with the same wavelet (k = 1.20, β = 1.5). The CC with the reference reaches its maximum (0.978) at k = 1.20, which coincides with the maximum of the spectral-match score of rule (1), and decreases to 0.855 at k = 1.0, 0.893 at k = 1.4 and 0.764 at k = 1.6 (Figure 7a), and the same optimum is obtained at

SNR = 10 dB (CC = 0.882). When the analysis wavelet deviates from the data's effective wavelet, BPDN compensates for the mismatch with additional atoms, which increases the spurious-event rate (from 2.5% at k = 1.2 to 10.2% at k = 1.4 and 25.7% at k = 1.6). Therefore, k should be selected from the data rather than fixed a priori. The optimal λ_r increases with the noise level (Figure 7b). The discrepancy principle (rule (2)) selected λ_r = 0.002, 0.002, 0.005 and 0.01 at SNRs of ∞, 20, 10 and 5 dB, respectively, which gave CC values within 0.01 of the best value on the grid in all cases. Too small a λ fits the noise, whereas too large a λ removes weak reflections and reduces the CC (e.g., to 0.76 at 10 dB for λ_r = 0.05).

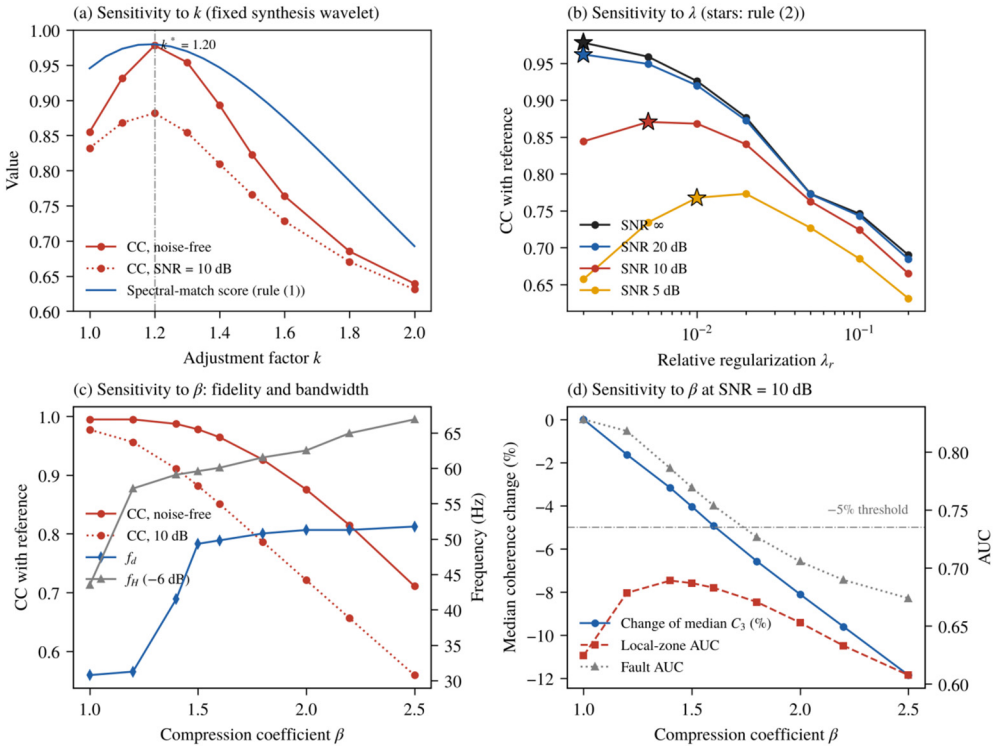


Figure 7. BPFE parameter sensitivity analysis: (**a**) CC with the reference (noise-free data, fixed synthesis wavelet) and spectral-match score of rule (1) versus k (the vertical dash-dotted line and k* = 1.20 mark the optimal value selected by rule (1)); (**b**) CC versus λ_r for different SNRs (stars mark the values selected by rule (2)); (**c**) CC, dominant frequency f_d and upper band limit f_H versus β; (**d**) change in the median coherence, local-zone AUC and fault AUC versus β at SNR = 10 dB.

β controls the trade-off between resolution and reliability (Figure 7c,d). For noise-free data, increasing β from 1.0 to 1.5 increases the dominant frequency from 30.8 to 49.3 Hz and decreases the tuning thickness from 16 to 11 ms, while the CC remains above 0.97. Beyond β = 1.6, the CC decreases (0.875 at β = 2.0) and the spurious-event rate increases (16.8% at β = 2.0). However, the dominant frequency hardly increases further, because the sparse reflectivity cannot support frequencies far beyond the original band. At SNR = 10 dB, the BPDN reconstruction without compression (β = 1) already improves the fault AUC from 0.740 to 0.828 because of its denoising effect. Increasing β trades part of this gain for vertical resolution, and the local-zone AUC reaches its maximum (0.687–0.689) at β = 1.4–1.5. The median coherence decreases by 4.0% at β = 1.5, 4.9% at β = 1.6 and 6.6% at β = 1.8 relative to β = 1. Therefore, rule (3) selects β = 1.6, which is close to the value of 1.5 used in the other tests (CC 0.851 versus 0.882 and local-zone AUC 0.683 versus 0.687). For noise-free data, the median coherence changes by less than 0.2% for all β, so the upper bound of rule (3) becomes active. This shows that the coherence criterion detects noise amplification but not prior-driven artifacts, which are instead controlled by the upper bound of β.

3.1.5. Comparison with Conventional Resolution-Enhancement Methods

BPFE was compared with four conventional methods, which were applied to the same data and shaped to the same target spectrum. The first was zero-phase spectral whitening (SW; 10 Hz smoothing window, 1% stabilization). The second was Wiener–Levinson spiking deconvolution (DC; 60 ms operator, 1% prewhitening, minimum-phase assumption), followed by a statistical correction of the residual phase and time shift. The third was stabilized inverse-Q filtering (IQ; stabilization factor $\sigma^2 = 10^{-3}$ [59]), which was applied to the attenuated data. The fourth was ℓ_1 sparse-spike reflectivity inversion with a statistically estimated zero-phase wavelet (SSRI), re-convolved with the target wavelet and regularized with the same rule (2). The results at SNR = 10 dB are listed in Table 3 (top: stationary data; bottom: attenuated data, $Q = 60$), and those of the attenuated data are shown in Figure 8.

Table 3. Comparison of BPFE with conventional resolution-enhancement methods.

Method	f_d (Hz)	−6 dB Band (Hz)	CC	SNR_r (dB)	Mean/RMS Phase (°)	Amp. err. (%)	Spur. (%)	Tuning (ms)	Fault AUC	Zone AUC
Stationary data										
Input	30.8	12.7–44.9	-	-	-	-	-	18	0.740	0.580
SW	39.6	21.0–59.6	0.843	5.4	0.9/9.5	19.2	35.9	16	0.743	0.658
DC	39.6	21.5–61.0	0.787	4.2	−16.1/38.9	25.8	41.7	14	0.729	0.600
SSRI	39.6	20.0–57.6	0.854	5.7	7.3/21.7	15.9	27.1	13	0.790	0.639
BPFE	48.8	25.4–60.5	0.882	6.5	4.5/26.2	17.1	23.4	14	0.769	0.687
Attenuated data ($Q = 60$)										
Input	23.4	11.7–41.5	-	-	-	-	-	18	0.754	0.577
SW	39.6	20.0–57.1	0.857	5.8	0.3/14.8	20.8	33.8	12	0.792	0.626
DC	39.1	20.5–57.6	0.788	4.2	−13.6/33.8	35.1	42.9	14	0.771	0.579
IQ	30.8	12.7–45.4	0.662	2.5	−0.2/7.9	11.4	61.8	18	0.689	0.568
SSRI	31.2	17.6–56.6	0.868	6.1	6.5/28.3	14.6	26.5	13	0.807	0.600
BPFE	48.3	36.1–59.1	0.853	5.6	4.9/24.3	43.1	24.6	14	0.790	0.646

SW, spectral whitening; DC, spiking deconvolution with residual phase correction; IQ, inverse-Q filtering (true Q; a 30% error in Q changed its CC by approximately 0.02); SSRI, sparse-spike reflectivity inversion. Amp. err., mean relative amplitude error of the key reflectors; Spur., spurious events; -, not applicable. CC, SNR_r, phase, amplitude and spurious-event metrics are computed with respect to the same ideal reference $r(t) * \omega(\beta t)$; the tuning thickness is obtained from the noisy wedge model. The upper and lower parts of the table list the results for the stationary and attenuated ($Q = 60$) data, respectively.

For the stationary data, BPFE gave the highest fidelity (CC = 0.882 and SNR_r = 6.5 dB, versus 0.787–0.854 and 4.2–5.7 dB for SW, DC and SSRI), the lowest spurious-event rate (23.4% versus 27.1–41.7%) and the highest local-zone AUC (0.687 versus 0.600–0.658), whereas SSRI gave a slightly higher fault AUC (0.790 versus 0.769). SW preserves the phase of the data best (RMS phase difference 9.5°), but it amplifies noise in the extended band; DC introduces a residual phase error (mean −16°) because the zero-phase wavelet violates the minimum-phase assumption. For the attenuated data, IQ restores the source band (CC = 0.86 with the unattenuated input) but does not extend the bandwidth beyond it, so that its tuning thickness remains 18 ms. BPFE again gave the highest local-zone AUC (0.646 versus 0.568–0.626) and a fault AUC similar to those of SW and SSRI (0.790 versus 0.792 and 0.807), but its CC (0.853) was slightly lower than those of SW (0.857) and SSRI (0.868), and the amplitudes of the deeper key reflectors were not compensated (mean error 43%), because the stationary analysis wavelet cannot account for the attenuation-related nonstationarity. Note that the synthetic wavelet is exactly zero-phase and stationary, which is the ideal situation for SW and SSRI. For field data, wavelet estimation errors would affect SSRI and DC but not BPFE, which requires only the average dominant frequency.

Overall, without wavelet estimation, BPFE achieves fidelity comparable to or better than that of the conventional methods and provides the best detectability of weak bed-confined discontinuities, whereas strongly attenuated data should be compensated or processed in time windows before BPFE is applied.

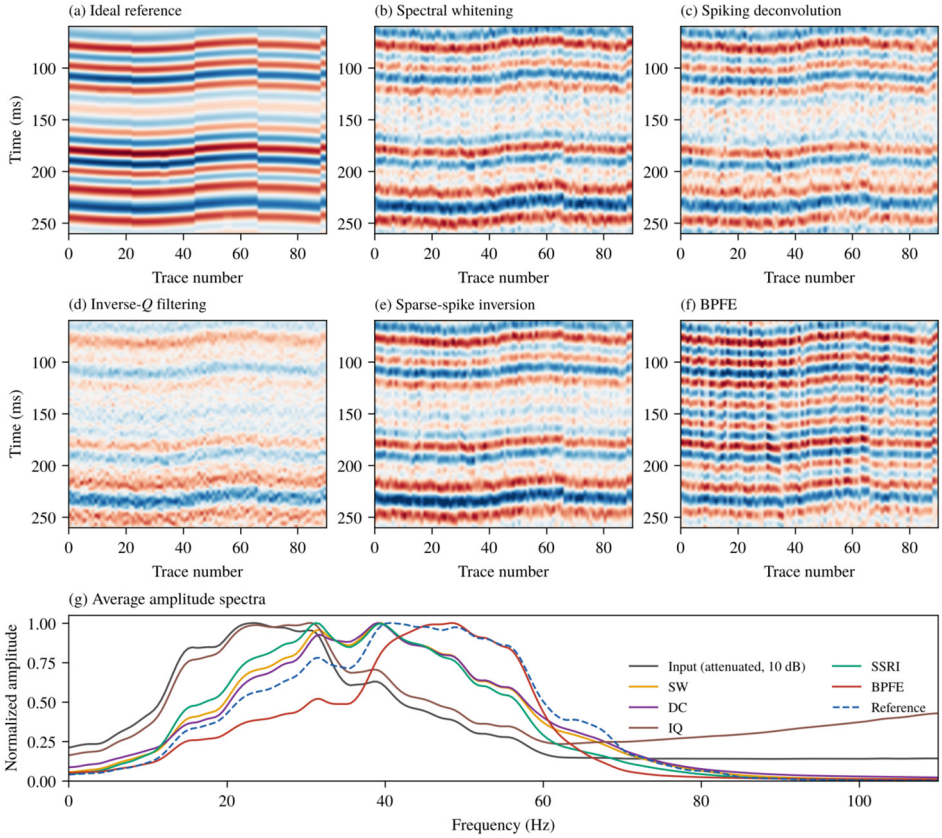


Figure 8. Comparison of resolution-enhancement methods for the attenuated data (Q = 60, SNR = 10 dB; traces 0–90, 60–260 ms): (**a**) ideal reference; (**b**) spectral whitening; (**c**) spiking deconvolution; (**d**) inverse-Q filtering; (**e**) sparse-spike inversion; (**f**) BPFE; (**g**) average amplitude spectra. In (**a**–**f**), red and blue denote positive and negative amplitudes, respectively; in (**g**), the line colors identify the methods, as indicated in the legend.

3.2. Field Data Application

3.2.1. Geological Setting

The Sichuan Basin, located at the northwestern margin of the Yangtze Plate and east of the Qinghai–Xizang Plateau, is a multi-cycle superimposed basin developed on the Upper Yangtze Craton [80]. The basin is rhombic in shape. It is bounded by the Micangshan Uplift and Dabashan Fold Belt to the north, the Daliangshan–Daloushan Fold Belt to the south, the Longmenshan Fold Belt to the west, and the eastern Sichuan fault-fold belt to the east [81] (Figure 9). In terms of tectonic evolution, the Sichuan Basin has successively experienced several key tectonic movements since the Neoproterozoic, including the Yangtze, Caledonian, Hercynian, Indosinian, Yanshanian and Himalayan cycles [82,83]. Across the northeastern Sichuan region, structural deformation becomes increasingly intense from southwest to northeast, and the degree of fault development gradually increases. The western Yuanba area shows a relatively gentle overall structure, whereas local strata are folded in the northwestern part near the Jiulongshan anticline. The Bazhong area, located east of Yuanba, contains local fault-fold belts with northwest-trending high-angle reverse faults, and a few faults vertically cut through the strata from the Lianggaoshan Formation to the Xujiahe Formation [84].

Multiple hydrocarbon-bearing intervals are vertically developed in the Jurassic succession of the northern Sichuan region, including the Zhenzhuchong and Dongyuemiao members of the Ziliujing Formation, as well as the Lianggaoshan and Shaximiao formations. From bottom to top, the Lianggaoshan Formation is divided into the Liang-1, Liang-2, and Liang-3 members. During the deposition of the Lianggaoshan Formation, a delta–lacustrine depositional system mainly developed in the northern Sichuan region. The distribution of sedimentary facies was influenced by sediment supply from the Micangshan Mountain in the north and Dabashan Mountain in the northeast [85]. Multi-stage channel sandstones are adjacent to lacustrine mudstones and shales, and the source rocks underlie the reservoir intervals, which provides favorable conditions for near-source hydrocarbon accumulation. The Lianggaoshan Formation is currently the most favorable exploration target for Jurassic tight sandstone oil and gas in the northeastern Sichuan region [84,86]. In recent years, important discoveries have been made in natural gas exploration of the Lianggaoshan Formation at selected locations in northeastern Sichuan, but no substantial breakthrough has yet been achieved across the broader area. Moreover, the test production of the wells is relatively low, which is inconsistent with the expected favorable accumulation conditions, indicating that reservoir prediction, especially fracture prediction, urgently needs to be improved.

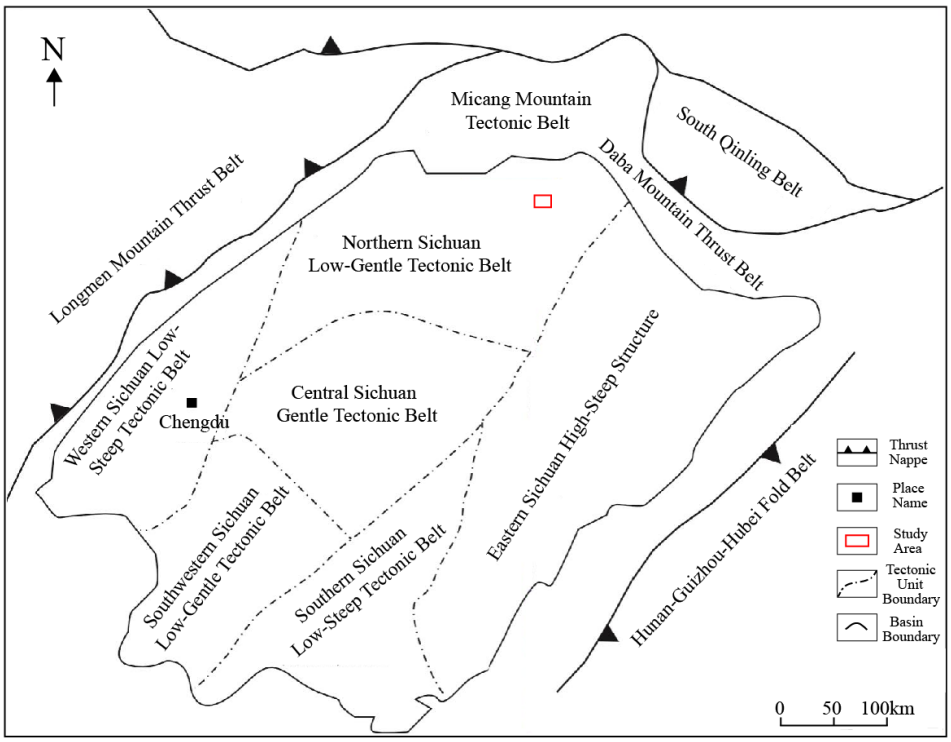


Figure 9. Structural location in the Sichuan Basin and its peripheral areas (modified from [87]).

3.2.2. Fracture Prediction Results

The third-generation eigenvalue coherence and ant-tracking techniques are used to extract coherence and ant-tracking attributes, respectively, for predicting the development and spatial distribution of faults and fractures. The results are shown in Figures 10 and 11. In coherence-based fracture prediction, high coherence values indicate high similarity between adjacent seismic traces, whereas low coherence values indicate low similarity. In the horizontal coherence slice in Figure 10, the white areas indicate high coherence values, which reflect good integrity of the medium and correspond to rock without fracture development. The black discontinuous line segments within the white areas represent

low coherence values. They reflect discontinuities and poor integrity of the medium and indicate possible faults and fracture zones. Figure 10 shows that the faults in the study area generally trend nearly east–west, and the boundaries, strikes and bifurcations of large faults are relatively clear. The largest fault trends northwest–southeast, penetrates the entire stratigraphic interval, and is associated with nearly east–west faults and fractures.

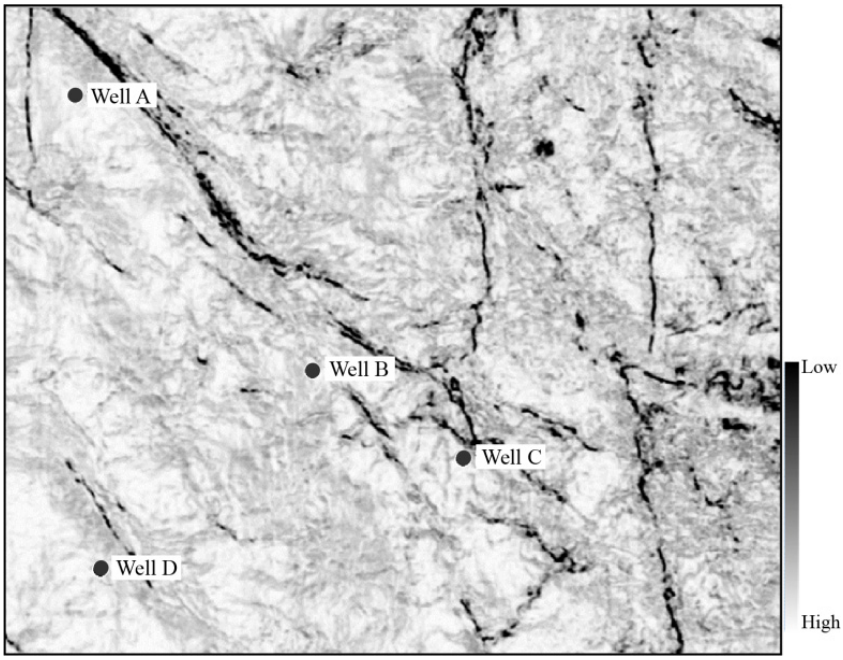


Figure 10. Fracture prediction results from the three-dimensional seismic coherence attribute.

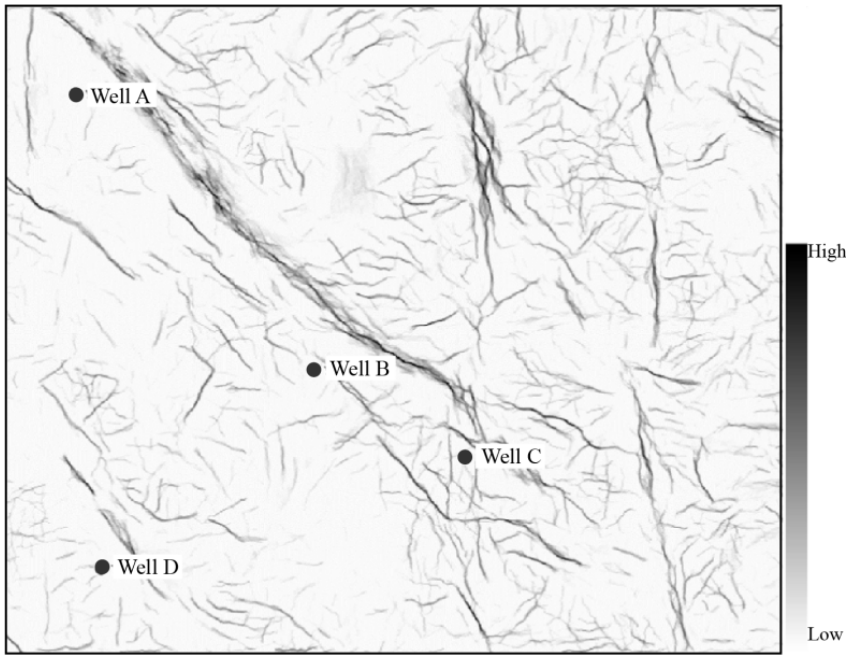


Figure 11. Fracture prediction results from the three-dimensional seismic ant-tracking attribute.

Compared with coherence attributes, ant-tracking attributes show fractures more clearly and in greater detail, and they have a stronger ability to characterize fracture development and distribution, especially for identifying small-scale fractures (Figure 11). Here, the ant-tracking attributes are obtained by applying ant tracking in Aggressive mode to the variance volume (see Table 1 for the parameters). The performance of ant tracking is

controlled by its parameter settings, including the ant boundary, ant track deviation, ant step size, number of allowed illegal steps, number of required legal steps and termination criteria. In practical applications, if each parameter is tested, compared, and optimized separately, thousands of parameter combinations may result, which requires substantial manpower and resources. Petrel software provides two preset parameter modes for ant tracking, namely, Aggressive and Passive. They differ mainly in the initial ant boundary and the threshold values used during the search. The Aggressive mode behaves like diligent ants with stronger initiative and is more suitable for tracking small- and medium-scale fractures. In contrast, the Passive mode behaves like lazy ants, which tend to track very strong signals and ignore weaker ones. This mode is more favorable for identifying large- and medium-scale faults. Note that because the Aggressive mode is sensitive to weak discontinuities, it may enhance not only genuine fractures but also local artifacts introduced by frequency extension.

As shown in Figures 10 and 11, coherence analysis and ant tracking generally perform similarly in characterizing faults and fractures, although clear differences exist. These differences mainly occur in the characterization of small-scale fractures and detailed features, indicating that different seismic attributes highlight fractures at different scales. Ant-tracking attributes show stronger continuity in characterizing small- and medium-scale faults and fractures and depict fracture details more clearly. In contrast, eigenvalue coherence attributes are less effective in describing small-scale fractures, but they have good practical value for identifying large-scale faults and fractures. The results of coherence analysis and ant tracking indicate that faults and fractures are relatively well developed within the reservoir in the study area, with irregular and complex fracture sizes and spatial distributions. Overall, fracture development is mainly controlled by the northwest–southeast maximum principal stress, and fractures along this direction are relatively well developed. At the same time, secondary small-scale fractures are also developed in some intervals, such as the north–south faults in the upper-right region of the study area. Note that these results refer to resolvable seismic discontinuities. Individual fractures with millimeter- to centimeter-scale apertures and lengths below the bin size are not resolved individually; instead, they are detected collectively as fracture zones that modify the seismic waveform.

Coherence attributes can characterize faults and relatively large-scale fractures with relatively high accuracy, whereas ant-tracking attributes can characterize relatively small-scale fractures. However, a single method is insufficient to fully describe the spatial distribution and complexity of a fault and fracture system. The small-scale fracture development probability volume obtained from ant tracking is weighted and fused with the large-scale fault and fracture probability volume obtained from coherence analysis, thereby achieving multi-attribute fusion-based multiscale fracture comprehensive prediction, as shown in Figure 12. Figure 12 further shows that faults and fractures are relatively well developed in the study area and exhibit clear multiscale characteristics and heterogeneity. Combining coherence analysis with the ant-tracking algorithm overcomes their individual limitations while retaining their respective advantages. As a result, fault and fracture features in the seismic data are captured more comprehensively, and the predicted fracture distribution is more consistent with the actual geological understanding. Coherence acts as the trend constraint in the fusion, so isolated ant-tracking responses that are not supported by coherence receive lower fracture probabilities. Nevertheless, newly appearing small-scale features should be interpreted together with their lateral continuity and their consistency with the structural framework.

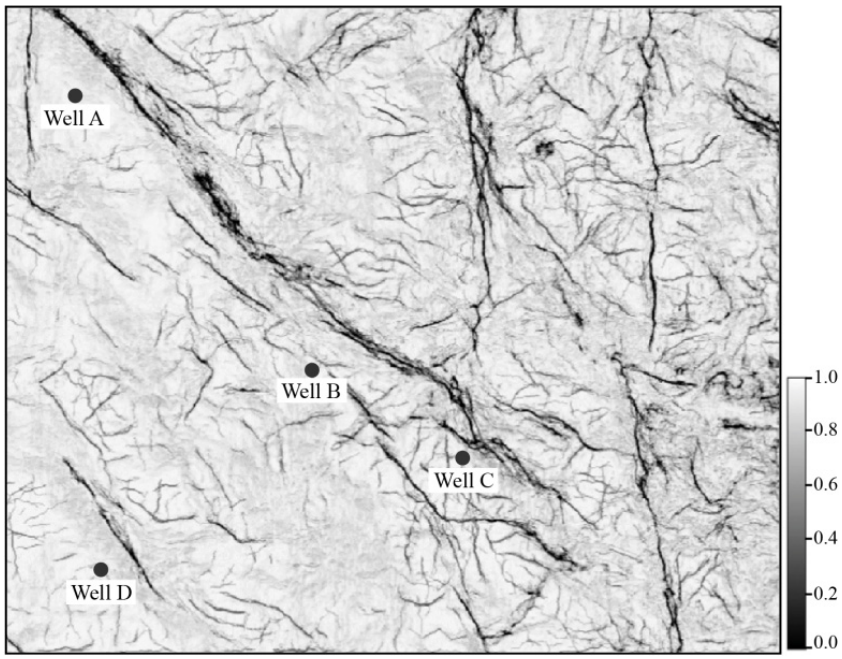


Figure 12. Fracture prediction results from the fusion of seismic coherence and ant-tracking attributes.

Reliable prediction of multiscale fractures is an important basis for improving the success rate of reservoir sweet-spot prediction, and the key lies in accurately predicting the development and spatial distribution of small-scale fractures. The BPFE method is first applied to the seismic data for frequency extension. Coherence and ant-tracking attributes are then extracted and fused to obtain the fracture prediction results shown in Figure 13. Figure 13 uses the same normalization, fusion weights and gray scale as Figure 12. After BPFE-based high-resolution processing, the seismic reflection events become narrower, reflection details increase, and energy becomes more balanced, thereby improving the ability of seismic data to identify small-scale fractures. A comparison of Figures 12 and 13 shows that fault and fracture detection using the BPFE-processed data provides a more refined image of small-scale fracture structures. In contrast, it has little influence on the detection of large-scale fractures. During fault formation, a series of secondary fractures are generated around faults under tectonic stress. Fractures in the target strata are mainly controlled by faults and folds, and the fault strikes are mainly northwest–southeast and north–south. Overall, small-scale fractures are relatively well developed and are mainly distributed near large-scale faults. Figure 13 shows that the areas around faults correspond well to fracture development zones, and the fracture orientation is generally consistent with the fault strike.

Among the four available wells, fractures are developed in wells A, B, and C, whereas fractures are poorly developed in well D. Figure 13 shows that fractures are well developed at wells A, B and C but relatively undeveloped at well D, which is consistent with the well-log interpretation results and the actual geological understanding. Fractures in the Lianggaoshan Formation are mainly controlled by faults and folds, and high-angle and oblique fractures are well developed. Among them, high-conductivity fractures mainly strike northwest–southeast and are developed in both sandstone and mudstone. Comparison with the oil and gas shows from mud logging indicates that multiple fractured gas-bearing intervals are interpreted in wells A, B and C. Fracture development can improve the storage and flow capacity of tight sandstones with poor matrix porosity. Wells A, B, and C all encountered gas-bearing layers in the target interval, but their gas production differed. Only wells B and C obtained commercial gas flow during testing. The well-log interpretation suggests that fractured gas-bearing layers are developed in the target

formation in wells B and C, and fracture development provides favorable conditions for hydrocarbon storage and migration. Because only four wells are available, these results are indicative rather than conclusive. As is well known, fracture development is a favorable but not a sufficient condition for productivity. Other factors, including the effective reservoir thickness, gas saturation, matrix porosity and permeability, completion and stimulation, and testing conditions, also control the test results. Therefore, the prediction results are used here only to evaluate whether fracture zones are correctly located at the wells, and the production differences among the wells are not attributed to fracture development alone.

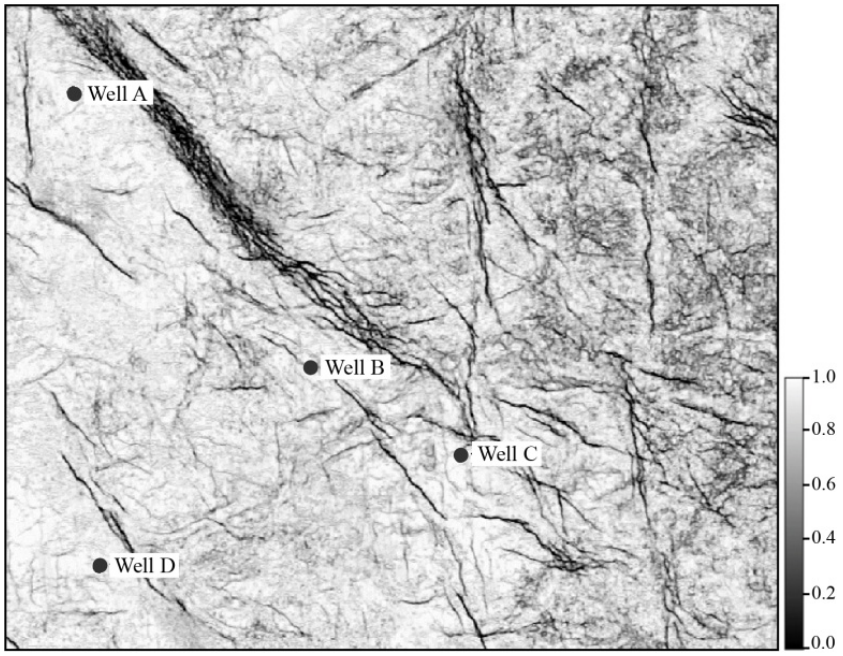


Figure 13. Fracture prediction results from basis pursuit frequency extension-enhanced coherence and ant-tracking attributes fusion.

4. Discussion

The BPFE method effectively broadens the seismic frequency band and enhances high-frequency energy and detailed information, and thus obtains more accurate and reliable fracture prediction results, especially for small-scale fractures. Compared with traditional high-resolution seismic processing methods, this method has the following characteristics: (1) It improves seismic data resolution by projecting records formed by low-frequency analysis-specific wavelets onto records formed by high-frequency synthetic wavelets. Although different low-frequency analysis wavelets and high-frequency synthetic wavelets are used, the wavelet family and the zero phase remain unchanged. Moreover, reconstruction using the BPDN only eliminates the sidelobe effects of the low-frequency analysis wavelets in the main seismic records. (2) The method uses BPDN, which accounts for noise in the model and is therefore adaptable to noisy data. In the synthetic tests, BPDN reduced the spurious-event rate relative to the noisy input by approximately one-third to one-half at SNRs of 5–20 dB (Figure 6c). (3) The method does not require estimation of the actual seismic wavelet, thereby avoiding a series of problems associated with seismic wavelet estimation. Meanwhile, because no actual wavelet is required, the relative spatiotemporal variations in seismic wavelets can be preserved, as can the wave-group characteristics and time-frequency properties of the seismic data. However, BPFE assumes approximately zero-phase and stationary input data within the processing window. When the analysis wavelet deviates from the effective seismic wavelet (e.g., when k is far from its optimum) or when the data are strongly nonstationary because of attenuation, the sparse

representation absorbs the mismatch. As a result, weak spurious events, timing jitter and uncompensated amplitude decay may occur. The output should therefore be regarded as a resolution-enhanced seismic image constrained by a sparse prior rather than as a true broadband record. Newly appearing high-frequency details should be interpreted together with their lateral continuity and geological plausibility.

Compared with conventional resolution-enhancement methods (Table 3), the main advantage of BPFE is not a larger bandwidth per se, because spectral whitening and deconvolution can produce a similar bandwidth when shaped to the same target. Instead, its advantage lies in the combination of three properties: no wavelet estimation is required, no systematic phase rotation is introduced, and BPDN suppresses noise that cannot be represented by the wedge dictionary. The last property results in fewer spurious events and better detectability of weak bed-confined discontinuities. Sparse-spike inversion with an accurately estimated wavelet performs similarly for through-going faults, but in field data its performance depends on the accuracy of the estimated wavelet phase, and it does not benefit from the dipole prior for thin layers. Inverse-Q filtering compensates for attenuation but does not extend the bandwidth beyond the source band. Because BPFE does not compensate for attenuation, the two methods are complementary. Therefore, for data with strong attenuation, inverse-Q filtering is recommended before BPFE (alternatively, BPFE can be applied in overlapping time windows).

Seismic coherence attributes directly measure the similarity between seismic signals and can effectively highlight discontinuities in the waveforms or amplitudes of multiple traces. They therefore perform well in predicting large- to medium-scale fractures. Ant tracking is an effective method for automatically tracking fracture trajectories. The resulting attributes can reduce the step-like artifacts caused by non-fault factors (e.g., stratigraphic stacking) in coherence attributes, thereby better characterizing small- and medium-scale fractures. However, these methods tend to highlight fractures at a single scale, and the mathematical independence of different fracture attributes presents a serious challenge for identifying an integrated fracture system. Fusing coherence and ant-tracking attributes can characterize faults and fractures in seismic data more comprehensively. After BPFE-based high-resolution processing, seismic reflection events become narrower and reflection details increase. Consequently, the correspondence between seismic attributes and fault and fracture zones with weak amplitude changes becomes more explicit. On this basis, multi-attribute fusion achieves more accurate and reliable fracture prediction, with a stronger ability to identify small-scale fractures and a clearer depiction of fracture details.

Other fracture-sensitive attributes can be incorporated into the fusion framework. Equation (23) can be generalized to $P_F = \Sigma_i \, w_i N(a_i)$ with $\Sigma_i \, w_i = 1$, where a_i may include, for example, the most-positive and most-negative curvatures, which are sensitive to flexure-related fractures in folds [30,31,36,37]. Curvature was not included in this study because the fractures in the target interval are mainly fault-controlled and parts of the study area are structurally gentle, where the assumed monotonic relationship between curvature and fracture intensity does not hold [13]. Moreover, second-derivative attributes are sensitive to noise and would be affected by the high-frequency components introduced by BPFE. A promising extension of the workflow, particularly in fold-related parts of the reservoir, is to integrate other fracture-sensitive attributes, such as curvature computed from the original data, with appropriate weights determined using a well-based criterion.

In summary, BPFE obtains sparse representations of seismic records using low-frequency analysis-specific wavelets and then reconstructs high-resolution seismic data using high-frequency synthetic analysis wavelets. This process extends the effective frequency band, enhances high-frequency energy and weak reflection details, narrows reflection events and sharpens local responses. These improvements are beneficial for identifying

small-scale fractures and fault-associated fracture zones. The third-generation eigenvalue coherence and ant-tracking attributes are complementary in scale. The former is sensitive to lateral discontinuities caused by faults and large- to medium-scale fractures and is suitable for characterizing the boundaries, strikes and bifurcations of main faults. The latter enhances fracture traces and is more advantageous for characterizing the continuity and detailed distribution of small- and medium-scale fractures. Attribute fusion based on attribute-sensitive scales not only preserves the stable characterization of large-scale faults by coherence but also enhances the fine characterization of small-scale fractures by ant tracking. It thus reveals the main controlling faults, secondary fractures and associated fracture zones more completely. The application results show that fractures are generally developed in the study area and are controlled by regional tectonic stress and fault activity. Their dominant orientations are northwest–southeast and nearly east–west, with locally developed north–south secondary fractures. Small-scale fractures are mostly distributed near large-scale faults, and their orientation is generally consistent with that of the main faults. The prediction results are consistent with the structural setting, fault distribution and well-log interpretation. They can provide a basis for reservoir sweet-spot prediction, well-location optimization and development planning.

Note that the fracture prediction in this study is mainly based on post-stack data, and the multi-azimuth gather information provided by wide-azimuth acquisition has not yet been fully used. Wide-azimuth seismic data can take advantage of pre-stack azimuthal resolution and are expected to overcome the limitations of post-stack attributes in terms of scale and accuracy. Future research may introduce pre-stack anisotropic information to supplement the details of fracture development and characterize weak seismic responses of fractures under the joint constraint of post-stack and pre-stack wide-azimuth data. In addition, seismic and well-log data are the main tools for fracture prediction. However, they describe fractures at very different scales, resulting in a scale gap between them. In the future, a fault and fracture prediction framework driven by multi-source information collaboration can be established by combining geological and geophysical knowledge with deep learning and by integrating image logs and rock physics constraints. Such a framework can more fully extract the small-scale fracture information hidden in seismic signals and bring the seismic prediction scale closer to the well-log scale, i.e., from tens of meters to the meter level. This would enable systematic and reliable characterization of fracture development and spatial distribution across different scales and types. Finally, the validation in this study is limited to synthetic tests and one field dataset from the Sichuan Basin. Although the synthetic tests covered different noise levels and attenuation, the applicability of the workflow to other basins, reservoir types and data qualities remains to be verified with independent field datasets.

5. Conclusions

A high-resolution multiscale seismic fracture prediction workflow based on basis pursuit frequency extension (BPFE)-enhanced multi-attribute fusion was proposed to characterize fracture systems that include main faults, fault-associated fracture zones and small-scale fractures. The main conclusions are as follows.

BPFE represents seismic traces sparsely on a wedge dictionary built from a zero-phase Morlet analysis wavelet and re-synthesizes them with a time-compressed wavelet, which extends the effective bandwidth without wavelet estimation. In tests with known reflectivity, BPFE reproduced the ideal high-resolution reference with CC = 0.978 for noise-free data and 0.882 at SNR = 10 dB. It also increased the dominant frequency from 30.8 to 49.3 Hz and reduced the tuning thickness from 16 to 11 ms without introducing systematic phase rotation.

Compared with spectral whitening, spiking deconvolution, inverse-*Q* filtering and sparse-spike inversion, BPFE gave comparable or higher fidelity, fewer spurious events and the best detectability of weak bed-confined discontinuities. However, its benefit decreases at low SNR, and strongly attenuated data should be compensated before BPFE is applied.

Coherence and ant tracking are sensitive to complementary attribute scales. Their normalized weighted fusion delineated main faults, fault-associated fracture zones and small-scale discontinuities in tight reservoirs more completely than either attribute alone. Moreover, the BPFE-enhanced multi-attribute fusion results were consistent with the actual geological understanding.

The predicted scales are attribute-sensitive seismic scales rather than physical fracture apertures or lengths, and the workflow has been validated with one field dataset only. Future work will apply it to other independent datasets, incorporate additional attributes such as curvature, and combine post-stack attributes with pre-stack wide-azimuth data, image logs and rock-physics constraints to characterize fracture properties such as filling, aperture and azimuthal anisotropy.

Author Contributions: Conceptualization, J.W. and Y.X.; methodology, J.W., J.C. and Y.X.; software, J.W. and Y.X.; validation, J.W. and Y.X.; formal analysis, J.W.; investigation, J.W., J.C. and Y.X.; resources, J.C. and Y.X.; writing—original draft preparation, J.W.; writing—review and editing, J.C. and Y.X.; visualization, J.W. and Y.X.; supervision, J.C.; project administration, J.W., J.C. and Y.X.; funding acquisition, J.W., J.C. and Y.X. All authors have read and agreed to the published version of the manuscript.

Funding: This research was funded by the National Natural Science Foundation of China, grant numbers 42330813, 42474145 and U24A20591, and the Natural Science Foundation of Sichuan Province, grant number 2026NSFSC1138.

Data Availability Statement: The field data used in this study are proprietary and cannot be shared publicly because of confidentiality agreements with the data owner. The processing parameters are listed in Table 1, and the BPFE algorithm is given as pseudocode in Algorithm 1. The synthetic models, the BPFE implementation and the scripts used for the synthetic tests are available from the corresponding author upon reasonable request. The intermediate attribute volumes (coherence, ant-tracking and fused fracture-probability slices) can be provided upon reasonable request, subject to approval by the data owner.

Conflicts of Interest: The authors declare no conflicts of interest.

References

1. Guo, Z.; Qin, X.; Liu, C. Pore and Microfracture Characterization in Tight Gas Sandstone Reservoirs with a New Rock-Physics-Based Seismic Attribute. *Remote Sens.* **2023**, *15*, 289. [CrossRef]
2. Lai, J.; Su, Y.; Dang, W.; Ju, Y.; Xin, Y.; Chen, K.; Zhang, Y.; Zhang, R.; Shan, X.; Zhao, Y.; et al. Well logging evaluation method of reservoir fractures. *Acta Pet. Sin.* **2025**, *46*, 2187–2210. [CrossRef]
3. Liu, J.; Ding, W.; Xiao, Z.; Dai, J. Advances in comprehensive characterization and prediction of reservoir fractures. *Prog. Geophys.* **2019**, *34*, 2283–2300.
4. Lai, J.; Liu, B.; Li, H.; Pang, X.; Liu, S.; Bao, M.; Wang, G. Bedding parallel fractures in fine-grained sedimentary rocks: Recognition, formation mechanisms, and prediction using well log. *Pet. Sci.* **2022**, *19*, 554–569. [CrossRef]
5. Li, S.; Zhao, Y.; Xian, C.; Liang, X.; Zhang, J.; Qiao, Q.; Yan, L.; Shen, Y.; Cao, H. Small-scale fracture detection via anisotropic Bayesian ant-tracking colony optimization driven by azimuthal seismic data. *IEEE Trans. Geosci. Remote Sens.* **2023**, *61*, 5920512. [CrossRef]
6. Ren, Q.Q.; Jin, Q.; Feng, J.W.; Li, Z.; Du, H. Geomechanical models for the quantitatively prediction of multi-scale fracture distribution in carbonate reservoirs. *J. Struct. Geol.* **2020**, *135*, 104033. [CrossRef]
7. Zeng, L.; Song, Y.; Han, J.; Han, J.; Yao, Y.; Huang, C.; Zhang, Y.; Tan, X.; Li, H. Control of structure and fluid on ultra-deep fault-controlled carbonate fracture-vug reservoirs in Tarim Basin, NW China. *Pet. Explor. Dev.* **2025**, *52*, 128–139. [CrossRef]

8. Ameen, M.S.; MacPherson, K.; Al-Marhoon, M.I.; Rahim, Z. Diverse fracture properties and their impact on performance in conventional and tight-gas reservoirs, Saudi Arabia: The Unayzah, South Haradh case study. *AAPG Bull.* **2012**, *96*, 459–492. [CrossRef]
9. Laubach, S.E.; Zeng, L.; Hooker, J.N.; Wang, Q.; Zhang, R.; Wang, J.; Ren, B. Deep and ultra-deep basin brittle deformation with focus on China. *J. Struct. Geol.* **2023**, *175*, 104938. [CrossRef]
10. Wang, Z. Progress in fracture predicting in oil and gas reservoirs. *J. Jilin Univ. Earth Sci. Ed.* **2026**, *56*, 469–482.
11. Liu, T.; Zhang, R. A machine learning-based hybrid model for fracture parameterization and distribution prediction in unconventional reservoirs. *Comput. Geotech.* **2024**, *168*, 106146. [CrossRef]
12. Pei, S.; Fan, T.; Shen, J.; Zhang, X.; Du, X. Multiscale fracture prediction in the weathering zone of metamorphic buried hills using Gaussian-weighted enhancement and MAD dynamic grading. *IEEE Trans. Geosci. Remote Sens.* **2026**, *64*, 4701414. [CrossRef]
13. Yin, X.; Ma, Z.; Xiang, W.; Zong, Z. Review of fracture prediction driven by the seismic rock physics theory (I): Effective anisotropic seismic rock physics theory. *Geophys. Prospect. Pet.* **2022**, *61*, 183–204.
14. Pan, X.; Li, X.; Huang, L.; Li, L.; Wang, P.; Liu, J. Estimation of fracture properties from azimuthal seismic data using convolution neural network. *IEEE Geosci. Remote Sens. Lett.* **2024**, *21*, 3002005. [CrossRef]
15. Lu, G.; Zeng, L.; Liu, G.; Chen, X.; Ostadhassan, M.; Du, X.; Chen, Y. Subsurface natural fracture identification using an integrated ensemble learning method. *IEEE Trans. Geosci. Remote Sens.* **2025**, *63*, 4700716. [CrossRef]
16. Li, X.; Pan, X.; Liu, H.; Xu, H.; Wang, P.; Liu, J. Seismic inversion for fracture properties using model-data dual-driven network. *IEEE Trans. Geosci. Remote Sens.* **2025**, *63*, 5918309. [CrossRef]
17. Du, X.; Fan, T.E.; Fan, P.J.; Ma, S.F.; Zhang, X.W. Seismic prediction method of multi-scale fracture zone for buried-hill fractured reservoir. *Chin. J. Geophys.* **2024**, *67*, 3184–3195. (In Chinese)
18. Liu, E.L.; Ding, P.B.; Zhang, F.; Huo, S.D.; Li, X.Y. Validation of azimuthal-anisotropy based fracture prediction methods using physical modeling seismic data. *Chin. J. Geophys.* **2025**, *68*, 2684–2702. (In Chinese)
19. Liu, Z.; Qu, S.; Sun, J.; Dong, N. Progress of seismic fracture characterization technology. *Geophys. Prospect. Pet.* **2012**, *51*, 191–198.
20. Wang, K.; Yin, X.Y.; Ma, Z.Q.; Li, K. Fault prediction method based on multi-azimuth coherence attribute. *Chin. J. Geophys.* **2023**, *66*, 3828–3839. (In Chinese)
21. Guo, Z.; Zhang, X.; Liu, C. An improved scheme of azimuthally anisotropic seismic inversion for fracture prediction in volcanic gas reservoirs. *IEEE Trans. Geosci. Remote Sens.* **2022**, *60*, 5917312. [CrossRef]
22. Bo, X.; Li, J.; Li, W.; Li, X.; Qiao, J.; Han, L.; Chen, X. Prediction of fracture parameters using azimuthal impedance based on an improved ellipse analysis method. *IEEE Trans. Geosci. Remote Sens.* **2025**, *63*, 5924612. [CrossRef]
23. Peng, H.; Zhao, J.; Qiu, Z.; Zhang, Q.; Liu, W.; Kong, W.; Gao, W.; Sheng, T.; Li, W.; Yang, Y. Multi-scale fracture characterization method for transitional shale reservoir based on post-stack multi-attribute ant-tracking fusion and pre-stack wide-azimuth gathers AVAZ analysis. *Geomech. Geophys. Geo-Energy Geo-Resour.* **2025**, *11*, 13. [CrossRef]
24. Pérez, M.A.; Gibson, R.L.; Toksöz, M.N. Detection of fracture orientation using azimuthal variation of P-wave AVO responses. *Geophysics* **1999**, *64*, 1253–1265. [CrossRef]
25. Barone, A.; Sen, M.K. A new Fourier azimuthal amplitude variation fracture characterization method: Case study in the Haynesville Shale. *Geophysics* **2018**, *83*, WA101–WA120. [CrossRef]
26. Liao, J.; Wen, P.; Xu, Y.; Zhou, L.; Liu, H.; Wang, L. An integrated study on fracture prediction using 3D P-wave field seismic data. *Geophysics* **2022**, *87*, B313–B328. [CrossRef]
27. Liu, H.; Pan, X.; Liu, Z.; Huang, L.; Li, X.; Liu, J. Azimuthal prestack seismic inversion for fracture parameters based on L1-2 norm regularization. *IEEE Trans. Geosci. Remote Sens.* **2024**, *62*, 5922410. [CrossRef]
28. Crampin, S. Evaluation of anisotropy by shear-wave splitting. *Geophysics* **1985**, *50*, 142–152. [CrossRef]
29. Zhang, X.; Li, Y.; Tang, J.; Yang, H.; Liu, Y. Using multi-wave data to detect fractures. *Oil Geophys. Prospect.* **2003**, *38*, 431–434, 438.
30. Chopra, S.; Marfurt, K.J. Volumetric curvature attributes add value to 3D seismic data interpretation. *Lead. Edge* **2007**, *26*, 856–867. [CrossRef]
31. Gao, D.L.; Di, H.B. Extreme curvature and extreme flexure analysis for fracture characterization from 3D seismic data: New analytical algorithms and geologic implications. *Geophysics* **2015**, *80*, IM11–IM20. [CrossRef]
32. Cui, Z.; Cheng, B.; Xu, T.; Niu, S. Reservoir fracture prediction method and application based on structure-oriented filtering and coherent attributes of gradient structure tensor. *Oil Geophys. Prospect.* **2021**, *56*, 555–563.
33. Zhao, T.; Yue, Y.; Chen, T.; Qian, F. 3D Seismic Attribute Conditioning Using Multiscale Sheet-Enhancing Filtering. *Remote Sens.* **2025**, *17*, 278. [CrossRef]
34. Zhang, G.; Huang, X.; Wu, L.; Huang, X.; Xu, Y.; Wu, H.; Tang, S. Seismic-based workflow for multi-scale and multi-stage fracture characterization in the Longmaxi Formation, Weiyuan Gas Field, Sichuan Basin. *Acta Geophys.* **2025**, *73*, 2391–2406. [CrossRef]
35. Wang, J.; Cao, J.; Chen, Q. Seismic-print analysis enhanced multiattribute fusion for fracture distribution prediction in tight reservoirs. *IEEE Trans. Geosci. Remote Sens.* **2026**, *64*, 5903713. [CrossRef]
36. Roberts, A. Curvature attributes and their application to 3D interpreted horizons. *First Break* **2001**, *19*, 85–100. [CrossRef]

37. Al-Dossary, S.; Marfurt, K.J. 3D volumetric multispectral estimates of reflector curvature and rotation. *Geophysics* **2006**, *71*, P41–P51. [CrossRef]
38. Bahorich, M.; Farmer, S. 3-D seismic discontinuity for faults and stratigraphic features: The coherence cube. *Lead. Edge* **1995**, *14*, 1053–1058. [CrossRef]
39. Gersztenkorn, A.; Marfurt, K.J. Eigenstructure-based coherence computations as an aid to 3-D structural and stratigraphic mapping. *Geophysics* **1999**, *64*, 1468–1479. [CrossRef]
40. Lyu, B.; Qi, J.; Li, F.Y.; Hu, Y.; Marfurt, K.J. Multispectral coherence: Which decomposition should we use? *Interpretation* **2020**, *8*, T115–T129. [CrossRef]
41. Chen, G.; Li, S.C.; Song, S.Y.; Li, Y.Y.; He, J.X.; Tang, T.M.; Zhu, F.Y.; Zhao, Y.; Lu, M.H. Multi-scale fracture prediction of shale oil reservoir driven by the combination of post-stack and pre-stack seismic data. *Chin. J. Geophys.* **2024**, *67*, 2830–2849. (In Chinese)
42. Li, Y.; Wang, J.; Yang, H.; Yan, Z.; Zheng, X. Fracture characterization using azimuthal AVO, ant-tracking, and curvature. In *SEG Technical Program Expanded Abstracts 2013*; Society of Exploration Geophysicists: Tulsa, OK, USA, 2013; pp. 388–392.
43. Hunt, L.; Reynolds, S.; Brown, T.; Hadley, S. Quantitative estimate of fracture density variations in the Nordegg with azimuthal AVO and curvature: A case study. *Lead. Edge* **2010**, *29*, 1122–1137. [CrossRef]
44. Dorigo, M.; Maniezzo, V.; Colorni, A. Ant system: Optimization by a colony of cooperating agents. *IEEE Trans. Syst. Man. Cybern. Part B Cybern.* **1996**, *26*, 29–41. [CrossRef] [PubMed]
45. Pedersen, S.I.; Randen, T.; Sønneland, L.; Steen, Ø. Automatic fault extraction using artificial ants. In *SEG Technical Program Expanded Abstracts 2002*; Society of Exploration Geophysicists: Tulsa, OK, USA, 2002; pp. 512–515.
46. Acuña-Uribe, M.; Pico-Forero, M.C.; Goyes-Peñafiel, P.; Mateus, D. Enhanced ant tracking: Using a multispectral seismic attribute workflow to improve 3D fault detection. *Lead. Edge* **2021**, *40*, 502–512. [CrossRef]
47. Li, N.; Wang, L.; Huang, S.; Zhu, S.; Shen, P.; Hao, J. 3D seismic fine structural interpretation in complex fault zones based on the high-definition ant-tracking attribute volume. *Oil Geophys. Prospect.* **2019**, *54*, 182–190.
48. Nosrati, A.; Mesbahi, F.; Kadkhodaie, A.; Sedghi, M.H. Optimized ant tracking algorithm for fault and fracture detection: A case study from a southern Iran oilfield. *J. Appl. Geophys.* **2025**, *243*, 105963. [CrossRef]
49. Zhang, J.W.; Huang, H.D.; Liu, T.; Zhang, C. Multiscale fractures characterization based on ant colony optimization and two-dimensional variational mode decomposition. *IEEE J. Sel. Top. Appl. Earth Obs. Remote Sens.* **2018**, *11*, 2562–2570.
50. Albesher, Z.; Kellogg, J.; Hafiza, I.; Saeid, E. Multi-attribute analysis using coherency and ant-tracking techniques for fault and fracture detection in La Florida Anticline, Llanos Foothills, Colombia. *Geosciences* **2020**, *10*, 154. [CrossRef]
51. Ouyang, M.; Shi, J.; Hu, T.; Xu, G.; Zhao, D. 3D frequency-division fracture prediction in shale gas reservoir in Weiyuan area, Sichuan Basin, China. *J. Chengdu Univ. Technol. Sci. Technol. Ed.* **2020**, *47*, 75–84.
52. Hale, D. Methods to compute fault images, extract fault surfaces, and estimate fault throws from 3D seismic images. *Geophysics* **2013**, *78*, O33–O43. [CrossRef]
53. Yuan, S.; Xu, Y.; Xie, R.; Chen, S.; Yuan, J. Multi-scale intelligent fusion and dynamic validation for high-resolution seismic data processing in drilling. *Pet. Explor. Dev.* **2025**, *52*, 680–691. [CrossRef]
54. Li, J. Seismic resolution enhancement based on matching pursuit algorithm. *Geophys. Prospect. Pet.* **2024**, *63*, 571–577.
55. Cao, S.; Sun, Y.; Chen, S. Challenges and solutions to high-resolution data processing for seismic exploration. *Coal Geol. Explor.* **2023**, *51*, 277–288.
56. Li, F.; Niu, W.; Liu, D.; Wang, Y.; Huang, Y. High-resolution seismic data processing method based on supervised deep learning. *Oil Geophys. Prospect.* **2024**, *59*, 702–713.
57. Peacock, K.L.; Treitel, S. Predictive deconvolution: Theory and practice. *Geophysics* **1969**, *34*, 155–169. [CrossRef]
58. Yuan, Y.; Li, Y.C.; Zhou, S.C. Multichannel statistical broadband wavelet deconvolution for improving resolution of seismic signals. *IEEE Trans. Geosci. Remote Sens.* **2021**, *59*, 1772–1783. [CrossRef]
59. Wang, Y. Inverse Q-filter for seismic resolution enhancement. *Geophysics* **2006**, *71*, V51–V60. [CrossRef]
60. Tian, G.; Zhao, Y.; Zhang, W.; Yang, C. The inverse Q filtering method based on a novel variable stability factor. *Geophysics* **2023**, *88*, V207–V214. [CrossRef]
61. Yilmaz, Ö. *Seismic Data Analysis: Processing, Inversion, and Interpretation of Seismic Data*, 2nd ed.; Society of Exploration Geophysicists: Tulsa, OK, USA, 2001.
62. Lu, W.; Ding, W.; Zhang, S.; Xiao, H.; Zhao, M. A high-resolution processing technique for 3-D seismic data based on signal sub-space decomposition. *Chin. J. Geophys.* **2005**, *48*, 896–901. [CrossRef]
63. Chopra, S.; Castagna, J.; Portniaguine, O. Seismic resolution and thin-bed reflectivity inversion. *CSEG Rec.* **2006**, *31*, 19–25.
64. Puryear, C.I.; Castagna, J.P. Layer-thickness determination and stratigraphic interpretation using spectral inversion: Theory and application. *Geophysics* **2008**, *73*, R37–R48. [CrossRef]
65. Zhang, R.; Castagna, J. Seismic sparse-layer reflectivity inversion using basis pursuit decomposition. *Geophysics* **2011**, *76*, R147–R158. [CrossRef]

66. Morlet, J.; Arens, G.; Fourgeau, E.; Giard, D. Wave propagation and sampling theory—Part I: Complex signal and scattering in multilayered media. *Geophysics* **1982**, *47*, 203–221. [CrossRef]
67. Elad, M.; Bruckstein, A.M. A generalized uncertainty principle and sparse representation in pairs of bases. *IEEE Trans. Inf. Theory* **2002**, *48*, 2558–2567. [CrossRef]
68. Chen, S.S.; Donoho, D.L.; Saunders, M.A. Atomic decomposition by basis pursuit. *SIAM Rev.* **2001**, *43*, 129–159. [CrossRef]
69. Donoho, D.L.; Tsaig, Y. Fast solution of $\ell 1$-norm minimization problems when the solution may be sparse. *IEEE Trans. Inf. Theory* **2008**, *54*, 4789–4812. [CrossRef]
70. Beck, A.; Teboulle, M. A fast iterative shrinkage-thresholding algorithm for linear inverse problems. *SIAM J. Imaging Sci.* **2009**, *2*, 183–202. [CrossRef]
71. Liu, L.; Liu, Y.; Liu, C.; Zheng, Z. Iterative seismic random noise suppression method based on compressive sensing. *Chin. J. Geophys.* **2021**, *64*, 4629–4643.
72. Li, C.; Liu, X.; Yu, K.; Wang, X.; Zhang, F. Debiasing of seismic reflectivity inversion using basis pursuit de-noising algorithm. *J. Appl. Geophys.* **2020**, *177*, 104028. [CrossRef]
73. Luo, Y.; Wang, Y.E.; AlBinHassan, N.M.; Alfaraj, M.N. Computation of dips and azimuths with weighted structural tensor approach. *Geophysics* **2006**, *71*, V119–V121. [CrossRef]
74. Chen, Q.; Cao, J.; Su, Z.; Xiang, T.; Fu, J. Multi-scale fracture prediction method based on OVT domain seismic data. *Prog. Geophys.* **2023**, *38*, 1084–1094.
75. Dalley, R.M.; Gevers, E.C.A.; Stampfli, G.M.; Davies, D.J.; Ruijtenberg, P.A.; Vermeer, G.J.O. Dip and azimuth displays for 3-D seismic interpretation. *First Break* **1989**, *7*, 86–95. [CrossRef]
76. Yang, L.; Wang, Y. Application and simulation of ant colony algorithm in continuous path prediction of dynamic network. *Comput. Sci.* **2021**, *48*, 485–490.
77. Widess, M.B. How thin is a thin bed? *Geophysics* **1973**, *38*, 1176–1180. [CrossRef]
78. Kallweit, R.S.; Wood, L.C. The limits of resolution of zero-phase wavelets. *Geophysics* **1982**, *47*, 1035–1046. [CrossRef]
79. Fawcett, T. An introduction to ROC analysis. *Pattern Recognit. Lett.* **2006**, *27*, 861–874. [CrossRef]
80. He, D.; Li, D.; Zhang, G.; Zhao, Z.; Fan, C.; Lu, R.; Wen, Z. Formation and evolution of multi-cycle superposed Sichuan Basin, China. *Chin. J. Geol.* **2011**, *46*, 589–606.
81. Wen, L.; Luo, B.; Wang, X.; Xie, J.; Ran, Q.; Pan, K.; Jin, Z.; Guan, X. New exploration fields and resource potential of continental tight oil and gas in Sichuan Basin. *Acta Pet. Sin.* **2025**, *46*, 77–88.
82. Liu, S.; Sun, W.; Zhong, Y.; Deng, B.; Song, J.; Ran, B.; Luo, L.; Han, K. Evolutionary episodes and their characteristics within the Sichuan marine Craton Basin during Phanerozoic Eon, China. *Acta Petrol. Sin.* **2017**, *33*, 1058–1072.
83. Guo, X.; Wei, Z.; Wang, W.; Xu, Z.; Pan, L.; Liu, Z.; Li, C.; Zeng, K.; Yang, S. Characteristics of oil and gas resources in the Sichuan Basin and prospects for high-quality gas production growth. *Nat. Gas. Ind.* **2025**, *45*, 40–52.
84. Li, C.; Li, M.; Pan, L. Exploration potential and favorable targets of channel sandstone in Jurassic Lianggaoshan Formation in northern Sichuan Basin. *Fault-Block Oil Gas. Field* **2025**, *32*, 55–62.
85. Cheng, D.; Zhang, Z.; Hong, H.; Zhang, S.; Qin, C.; Yuan, X.; Zhang, B.; Zhou, C.; Deng, Q. Sequence structure, sedimentary evolution and their controlling factors of the Jurassic Lianggaoshan Formation in the East Sichuan Basin, SW China. *Pet. Explor. Dev.* **2023**, *50*, 262–272. [CrossRef]
86. Hu, D.; Li, Z.; Wei, Z.; Duan, J.; Liao, Z.; Pan, L.; Li, C.; Duan, H. Breakthrough in oil and gas exploration of Jurassic channel sandstone in Well Bazhong 1HF in northern Sichuan Basin and its significance. *Nat. Gas. Ind.* **2023**, *43*, 1–11.
87. Zhong, X.; Lin, L.; Yu, Y.; Wang, W.; Xia, W.; Li, C.; Nan, F.; Li, J. Comparative study of reservoir characteristics and porosity development factors of tight sandstone reservoirs in the Lower Jurassic Lianggaoshan Formation in the northern Sichuan Basin. *Mineral. Petrol.* **2025**, *45*, 171–185.

Disclaimer/Publisher's Note: The statements, opinions and data contained in all publications are solely those of the individual author(s) and contributor(s) and not of MDPI and/or the editor(s). MDPI and/or the editor(s) disclaim responsibility for any injury to people or property resulting from any ideas, methods, instructions or products referred to in the content.